Macrophage-NLRP3 Activation Promotes Right Ventricle Failure in Pulmonary Arterial Hypertension

Running Title: RVF in PAH is Driven by Macrophage Inflammasome Activation

Ruaa Al-Qazazi[1*], Patricia D. A. Lima[1,2*], Sasha Z. Prisco[3], Francois Potus[1,4], Asish Dasgupta[1], Kuang-Hueih Chen[1], Lian Tian[1,6], Rachel E. T, Bentley[1], Jeff Mewburn[1], Ashley Y. Martin [1], Danchen Wu[1], Oliver Jones[2], Donald H. Maurice[5], Sebastien Bonnet[4], Steeve Provencher [4], Kurt W. Prins[3], Stephen L. Archer[1,2**]

1- Department of Medicine, Queen's University, Kingston, Ontario, Canada
2- Queen's Cardiopulmonary Unit, Queen's University, Kingston, Ontario, Canada
3- Lillehei Heart Institute, Cardiovascular Division, University of Minnesota Medical School, Minneapolis, USA
4- Pulmonary Hypertension Research Group, Institut Universitaire de Cardiologie et de Pneumologie de Québec Research Center, Laval University, Quebec City, Quebec, Canada
5- Department of Biomedical and Molecular Science, Queen's University, Kingston, Ontario, Canada.
6- St. Strathclyde Institute of Pharmacy and Biomedical Sciences, University of Strathclyde, Glasgow, UK

* Equal contribution

** Corresponding author

Correspondence: Stephen L. Archer MD. FRCP(C), FAHA, FACC, FRSC
Elizabeth Smith Distinguished University Professor
C. Franklin and Helene K. Bracken Chair
Professor & Head Department of Medicine, Queen's University
Etherington Hall, Room 3041
94 Stuart St., Kingston, Ontario, Canada, K7L 3N6
E-mail : stephen.archer@queensu.ca
Telephone: 613 533-6327; Fax: 613 533-6695

AJRCCM Articles in Press. Published June 14, 2022 as 10.1164/rccm.202110-2274OC

Author's contributions to the study

A) Substantial contributions to the conception or design of the work; or the acquisition, analysis, or interpretation of data for the work: SLA, RQ, PDAL, KWP, SZP, FP, AD, KHC, LT, RB, JM, AM, DW, OJ, DHM, SB, SP
B) Drafting the work or revising it critically for important intellectual content: RQ, PL, SLA, KWP, FP, DW, DHM, SB, SP
C) Final approval of the version to be published: All authors
D) Agreement to be accountable for all aspects of the work in ensuring that questions related to the accuracy or integrity of any part of the work are appropriately investigated and resolved: All authors

Sources of funding:

This study was supported, in part, by the U.S. National Institutes of Health (NIH) grants NIH R01HL113003 (S.L. Archer) and NIH R01HL071115 (S.L. Archer), Canada Foundation for Innovation 229252 and 33012 (S.L. Archer), Tier 1 Canada Research Chair in Mitochondrial Dynamics and Translational Medicine 950-229252 (S.L. Archer), the William J. Henderson Foundation (S.L. Archer), the William M. Spear Endowment Fund in Pulmonary Research (Health Sciences Internal Grant Competition 2019) (D. Maurice, P.D.A. Lima) and the Mohammed Family PHA Canada scholarship (R. Al-Qazazi). S.Z.Prisco is funded by NIH F32 HL154533, NIH T32 HL144472, a University of Minnesota Clinical and Translational Science Award (NIH UL1 TR002494), and a University of Minnesota Medical School Academic Investment Educational Program Grant K.W.Prins is funded by NIH K08 HL140100, the Cardiovascular Medical Research and Education Fund, a Lillehei Heart Institute Cardiovascular Seed Grant, the University of Minnesota Faculty Research Development Grant, and the United Therapeutics Jenesis Award.

Disclosures: None

What is the Current Scientific Knowledge on this Subject

Pulmonary arterial hypertension (PAH) often results in death from right ventricular failure (RVF). The current dogma suggests that the transition from compensated to decompensated RVH is primarily a consequence of progression in pulmonary vascular disease and RV afterload. Our work challenges this dogma and suggests a critical role of RV inflammation in controlling adverse RV remodelling and dysfunction in PAH.

What Does This Study Add to the Field

The findings of this research reveal the pathological importance of the NLRP3 inflammasome activation pathway in right ventricular (RV) macrophages for the progression of Pulmonary Arterial Hypertension (PAH) to RV failure (RVF). We challenge the conventional view that RVF is primarily caused by increased PVR by treating RV inflammation with therapies targeting to reduce RV-macrophage accumulation (GP130 antagonist, SC-144) and NLRP3 inflammasome activation (MCC950), independent of the pulmonary vasculature.

AJRCCM Articles in Press. Published June 14, 2022 as 10.1164/rccm.202110-2274OC

Abstract

Rationale: Pulmonary arterial hypertension (PAH) often results in death from right ventricular failure (RVF). NLRP3-macrophage activation may promote RVF in PAH.

Objectives: Evaluating the contribution of the NLRP3 inflammasome in RV-macrophages to PAH-RVF.

Methods: Rats with decompensated RV hypertrophy (RVH) [monocrotaline (MCT) and Sugen-5416 hypoxia (SuHx)] were compared with compensated RVH rats [pulmonary artery banding (PAB)]. Echocardiography and right heart catheterization were performed. Macrophages, atrial natriuretic peptide (ANP) and fibrosis were evaluated by microscopy or flow cytometry. NLRP3 inflammasome activation and cardiotoxicity were confirmed by immunoblot and *in vitro* strategies. MCT-rats were treated with SC-144 (a GP130 antagonist) and MCC950 (an NLRP3 inhibitor). Macrophage-NLRP3 activity was evaluated in PAH-RVF patients.

Measurements and Main Results: Macrophages, fibrosis, and ANP were increased in MCT and SuHx-RVs but not LVs or PAB rats. While MCT-RV macrophages were inflammatory, lung macrophages were anti-inflammatory. $CCR2^{+}$ macrophages (monocyte-derived) were increased in MCT- and SuHx-RVs and highly expressed NLRP3. The macrophage-NLRP3 pathway was upregulated in PAH patients' decompensated RVs. Cultured MCT-monocytes showed NLRP3 activation, and in co-culture experiments resulted in cardiomyocyte mitochondrial damage, which MCC950 prevented. *In vivo*, MCC950 reduced NLRP3 activation and regressed pulmonary vascular disease and RVF. SC-144 reduced RV-macrophages and NLRP3 content, prevented STAT3 activation, and improved RV function without regressing pulmonary vascular disease.

AJRCCM Articles in Press. Published June 14, 2022 as 10.1164/rccm.202110-2274OC

Conclusion: NLRP3-macrophage activation occurs in the decompensated RV in preclinical PAH models and PAH patients. Inhibiting GP130 or NLRP3 signaling improves RV function. The concept that PAH-RVF results from RV inflammation rather than solely from elevated RV afterload suggest a new therapeutic paradigm.

Key Words: interleukin-1β (IL1β), mitochondrial fission, CCR2, SC-144, MCC950

AJRCCM Articles in Press. Published June 14, 2022 as 10.1164/rccm.202110-2274OC

Nonstandard Abbreviations and Acronyms	
ANP	Atrial natriuretic peptide
ARG1	Arginase 1
ASC	Apoptosis-associated speck-like receptor containing a CARD
CASP1	Caspase 1
CCR2	C-C chemokine receptor type 2
EF	Ejection Fraction
GP130	Glycoprotein 130
GSDMD	Gasdermin D
IL1β	Interleukin-1β
IL6	Interleukin-6
MCT	Monocrotaline
NLRP3	Nucleotide-binding domain, leucine-rich-containing family, pyrin domain-containing-3
NOS2	Nitric Oxide Synthase 2
P-STAT3	Phospho-Signal transducer and activator of transcription 3
PAAT	Pulmonary artery acceleration time
PAB	Pulmonary artery banding
PAH	Pulmonary Arterial Hypertension
RHC	Right heart catheterization
RVEDP	Right ventricular end-diastolic pressure
RVF	Right ventricular failure

AJRCCM Articles in Press. Published June 14, 2022 as 10.1164/rccm.202110-2274OC

RVFWT	Right ventricular free wall thickness
RVSP	Right ventricular systolic pressure
SuHx	Sugen-5416/ hypoxia
TAPSE	Tricuspid annular plane systolic excursion

AJRCCM Articles in Press. Published June 14, 2022 as 10.1164/rccm.202110-2274OC

Introduction

Pulmonary arterial hypertension (PAH) is a cardiopulmonary syndrome defined by an increased resting mean pulmonary artery pressure (mPAP >20 mmHg) and pulmonary vascular resistance (PVR >3 Wood units)[1]. The RV initially adapts to increased pressure by compensatory right ventricular hypertrophy (RVH) and increased RV contractility[2]. Eventually, these compensatory mechanisms are insufficient, leading to RV failure (RVF)[3-4]. The current dogma suggests that the transition from compensated to decompensated RVH is primarily a consequence of progression in pulmonary vascular disease and RV afterload.

PAH clinical trials and preclinical studies indicate that immune mediators play a crucial role in the pathogenesis of PAH[5-6]. Inflammatory cytokines such as IL1β and IL6 are elevated in the blood of PAH patients, and their levels correlate with disease severity and mortality[7-8]. Macrophages are amongst the primary effectors of inflammation in pulmonary vascular lesions in PAH and may aggravate disease severity[6,9]. Macrophages display remarkable plasticity in response to the environment[10], and can either be polarized to produce pro-inflammatory cytokines (M1) or function as anti-inflammatory cells (M2), promoting tissue repair. However, whether their accumulation contributes to impaired RV function remains unknown.

This study evaluates RV inflammation as an independent and therapeutically tractable cause of RVF. More specifically, this study assesses the role of the nucleotide-binding domain, leucine-rich-containing family, and pyrin domain-containing protein 3 (NLRP3) inflammasome in PAH. The NLRP3 inflammasome responds to the host damage-associated molecular patterns (DAMPs) by generating pro-inflammatory cytokines, notably IL1β[11]. When activated, NLRP3 recruits

AJRCCM Articles in Press. Published June 14, 2022 as 10.1164/rccm.202110-2274OC

apoptosis-associated speck-like protein containing a CARD (ASC). The assembled NLRP3:ASC complex recruits and activates caspase1 (CASP1), which is essential for the cleavage of IL1β and Gasdermin D (GSDMD), a pore-forming protein that participates in the release of active-IL1β and induction of pyroptosis[12-13]. We hypothesize that RV inflammation, driven by activation of the NLRP3 inflammasome in macrophages, is a significant contributor to RVF in PAH.

We have already reported preliminary results of this study in the form of abstracts[14,15]and showed that in PAH, there is RV-specific activation of NLRP3 in macrophages associated with RV decompensation, which is rescued through the inhibition of the NLRP3 pathway. This work suggests RV inflammation due to activation of the macrophages-NLRP3 inflammasome pathway and identifies new therapeutic targets for PAH, including much-needed therapies for RVF.

Methods

The authors declare that all supporting data are available within the article and the online-only Supplemental Data.

Experimental Animals

Experiments were conducted following the Canadian Council on Animal Care (CCAC) regulations approved by Queen's University Animal Care Committee (Protocol #1714, #1971 and #2112) or the University of Minnesota Institutional Animal Care and Use Committee (IACUC) (protocol # 1904-36927A).

Male Sprague-Dawley (SD) rats (Charles River, Sherbrooke, CA) were used to create all models. The PAB model used surgical banding of the pulmonary trunk with metal clips in rats at age 6-7 weeks (~115g)[16] (**Supplemental Methods).** The monocrotaline (MCT) model was created using a single subcutaneous injection of 60 mg/kg MCT in 8-9 weeks old rats (~250g)[17]. The Sugen-

AJRCCM Articles in Press. Published June 14, 2022 as 10.1164/rccm.202110-2274OC

5416 hypoxia (SuHx) model was created by a single subcutaneous injection of Sugen-5416 (20 mg/kg) in rats at the age of 8-9 weeks old (~250 g) combined with environmental hypoxia (10% normobaric hypoxia) for 3 weeks followed by 3 weeks of normoxia.

On day 14 post-MCT, rats received a daily injection of either SC-144 (10 mg/kg; intraperitoneally; APExBio Technology, Houston, TX); or MCC950 (6 mg/kg, intravenously; InvivoGen, CP-456773; San Diego, CA)[18].

Human samples

Control and decompensated human RV tissue were provided by the Institut de Cardiologie et de Pneumologie de Québec - Laval University (Canada), in accordance with the Comités d'éthique de la recherche (CÉR20775). The samples were obtained via autopsy or surgery. Patient information is summarized in **Table 1** and **Supplemental Table 3.**

Cardiac Assessment

RVF and response to therapy were assessed using high-resolution Doppler ultrasound (Vevo 2100, Visual Sonics, Toronto, ON) and closed-chest right heart catheterization (RHC; Scisense pressure-volume catheter; Transonic, London, ON) (**Supplemental Methods)**.

Tissue and cell processing

RV and lung tissue were prepared for immunohistochemistry, flow cytometry or western blotting. Peripheral blood mononuclear cells (PBMC) were evaluated via flow cytometry or used to obtain enriched monocytes tested in *vitro* for the activation of NLRP3 or co-cultured with rat neonatal cardiomyocytes (R-CM-561, Lonza, Basel Switzerland). Cardiomyocytes were assessed

AJRCCM Articles in Press. Published June 14, 2022 as 10.1164/rccm.202110-2274OC

for number, size, mitochondria fragmentation and membrane potential (**Supplemental Methods**; **Supplemental Table 1**).

Statistical Analysis

Randomization of experimental animals was implemented as per Provencher et al. 2018[19]. Results are presented as mean±IQR. Using GraphPad Prism (GraphPad Software, La Jolla, CA), One-way ANOVA or Student's *t*-test were used when the sample size was ≥8, and Mann-Whitney or Kruskal-Wallis tests were used when the sample size was ≤8. Two-way ANOVA was used to assess intergroup differences. A *p*-value <0.05 was considered statistically significant.

Results

An increase in RV-macrophage number is associated with reduced RV function and increased fibrosis in MCT-PAH and SuHx-PAH

RVH was present in both MCT (4-weeks) and PAB models compared to their respective controls. RVH was evident by increased RV free wall thickness (RVFWT) via echocardiography (*p=0.0006* and *p=0.0003*, respectively; **Table 2**) and shown on transverse histological sections of the heart (**Supplemental Figure 1A and B)**. Relative to controls, tricuspid annular plane systolic excursion (TAPSE) was significantly decreased in MCT but not in PAB rats **(***p=0.0012*; **Table 2**). Cardiac Output (CO) and Pulmonary Artery Acceleration Time (PAAT) were decreased in the MCT 3-weeks (*p=0.013* and *p=0.01,* respectively)*,* and both parameters were worse in MCT 4-weeks group compared to controls (p=*0.0006* and *p=0.0012,* respectively). Cardiac ultrasound was not conducted in the SuHx model. The Fulton index (RV/ LV+septum weight ratio) was increased in MCT-RV and PAB-RV compared to respective controls (*p=0.004* and *p=0.022*, respectively; **Table 2).**

AJRCCM Articles in Press. Published June 14, 2022 as 10.1164/rccm.202110-2274OC

RHC revealed elevated right ventricular systolic pressure (RVSP) in MCT (3- and 4-weeks), SuHx and PAB rats compared to controls (*p=0.009, 0.0007, 0.0043 and 0.0012*, respectively; **Table 2 and Supplemental Table 2**). In 4-weeks MCT and SuHx rats, CO, and ejection fraction (EF) were decreased (CO: MCT *p=0.0006,* SuHx *p=0.0159;* and EF: MCT *p= 0.0007,* SuHx *p=0.0036*) while right ventricular end-diastolic pressure (RVEDP) was increased (MCT: *p=0.0007,* SuHx*: p=0.015*) (**Table 2**). Compared to control, RVEDP was also increased in MCT 3-weeks (*p=0.009*). Cardiac index (CI) decreased significantly in 4-weeks MCT group only (*p=0.025*). Pressure-volume loops are shown in **Supplemental Figure 2A**. Although the CO significantly decreased in MCT 3-weeks compared to PBS as measured by cardiac ultrasound, there was no significant change in CO as measured by pressure-volume loops using closed chest RHC.

Atrial natriuretic peptide (ANP) expression was increased in MCT-RV compared to control-RV (*p=0.0067;* **Figure 1A; Supplemental Figure 3A)**. ANP expression in MCT-LV, PAB (RV and LV) and SuHx (RV and LV) was not significantly different from control (**Figure 1A**; **Supplemental Figure 3A***)*. Collagen deposition (as measured using Picrosirius Red) was increased in the MCT- and SuHx-RVs compared to their controls; but was not significantly increased in the PAB RVs (MCT *p<0.0001* and SuHx *p=0.0078;* **Figure 1A**). Collagen-III expression was also greater in MCT- and SuHx-RVs compared to control RVs (*p<0.0001 and p=0.0071,* respectively*)* but was not increased in PAB-RV, MCT-LV, or SuHx-LV, relative to their respective controls (**Figure 1A; Supplemental Figure 3B)**.

In situ quantification of macrophages ($CD68^+$ cells) via confocal microscopy showed a 5-fold increase in the MCT-RV compared to PBS-RV (105±19 *vs.* 19±3 macrophages/0.3025 $mm^{2,}$ respectively; *p<0.0001;* **Figure 1B**). A similar 4-fold increase in RV-macrophages was observed in SuHx rats (*p<0.0001;* **Figure 1B**). In contrast, there were no differences in macrophage numbers in

AJRCCM Articles in Press. Published June 14, 2022 as 10.1164/rccm.202110-2274OC

PAB-RV compared to sham-RV (17±2 and 12±2 macrophages/0.3025 mm^2, respectively; **Figure 1B)**. This indicates that compensated RVH alone was not associated with RV macrophage infiltration in our PAB model. The macrophage accumulation in PAH was RV-specific, with no increase in LV macrophages in either MCT or SuHx relative to control LVs (**Supplemental Figure 3C)**. Further characterization demonstrated that in the RV, monocyte-derived ($CCR2^+$) and tissue-resident macrophages ($CCR2^-$) were present. Both subsets of macrophages were significantly increased in MCT and SuHx rats relative to controls. While the monocyte-derived macrophages were the predominant population in MCT rats ($CCR2^+$: 57.77±27.56 *vs.* $CCR2^-$: 33.93±10.66 macrophages per 0.3025mm^2), in SuHx rats, monocyte-derived and tissue-resident macrophages had similar incidence ($CCR2^+$: 17.40±2.48 *vs*. $CCR2^-$: 22.39±2.74 per 0.3025mm^2). The number of both macrophage subsets were lower in PBS and VeNx (PBS: $CCR2^+$: 0.56±0.38 *vs.* $CCR2^-$: 1.30±0.49 macrophages per 0.3025mm^2; VeNx: $CCR2^+$: 5.44±2.14 *vs.* $CCR2^-$: 3.67±0.68) compared to numbers in either PAH model (**Figure 1C**). Total $CCR2^+$ cells were significantly more abundant in MCT- and SuHx-RVs compared to controls (**Supplemental Figure 4A**), and the monocyte-derived macrophages (defined as cells that were positive for both CD68 and CCR2) were the predominant migratory leukocyte representing 54.7% (MCT) and 47.5% (SuHx) from the total $CCR2^+$ cells in the tissue (**Supplemental Figure 4B**).

Using flow cytometry, we were also able to identify and quantify RV-macrophage abundance, defined as the % of $CD68^+$ within the total of $CD45^+$ live cells. In this experiment, MCT rats treated for 3- and 4-weeks were compared, and it was further confirmed that there was a significant increase in $CD68^+$ cells in MCT-RVs compared to control-RVs (3-weeks: 45.5% in MCT *vs.* 35.3% in controls and 4-weeks: 74% in MCT *vs.*58.40% in controls). Pulmonary hypertension severity progressed between 3- to 4-weeks post-MCT, and the number of RV macrophages

AJRCCM Articles in Press. Published June 14, 2022 as 10.1164/rccm.202110-2274OC

significantly increased in parallel **(**3-weeks *vs.* 4-weeks MCT**:** *p=0.0095***; Figure 1D),** and this was associated with deterioration in RV function in MCT rats **(Table 2).** We also detected an inverse correlation between CO and macrophage abundance that was more evident at 4 weeks (r^2*=0.483*, *p=0.0173*) than 3-weeks (r^2*=0.293*, *p=0.165)* post-MCT treatment (**Figure 1E**). In contrast, despite RVH, the number of macrophages was unchanged in PAB *vs.* sham RVs (**Figure 1D).**

The macrophages in MCT and SuHx RV demonstrate NLRP3 inflammasome activation

We used flow cytometry to detect the baseline NLRP3 expression in RV cells. NLRP3 expression was 2-fold higher in macrophages than in other immune cells ($CD45^+CD68^-$; *p=0.0286*), endothelial cells ($CD45^-CD68^-CD90^-CD31^+$; *p=0.0286*), or fibroblasts ($CD45^-CD68^-CD31^-CD90^+$; *p=0.0286*; **Figure 2A**). No differences were detected in the expression of ARG1 (an anti-inflammatory M2 marker) in MCT-RV *vs.* control-RV macrophages (**Supplemental Figure 5)**, consistent with the polarization of RV macrophages toward an inflammatory M1 phenotype. To confirm the expression of NLRP3 in the RV-macrophages as well as its fluctuation after PAH development, we quantified the number of $NLRP3^+CD68^+$ macrophages (relative to total $CD68^+$ macrophages) in MCT and SuHx rats. Macrophages expressing NLRP3 were significantly increased in MCT- and SuHx-RVs compared to controls (*p=0.011* and *p=0.007*, respectively; **Figure 2B**), and no intergroup differences were observed.

Immunoblotting showed significantly higher NLRP3 expression in the MCT-RV (*p=0.036*), but not PAB-RVs, compared to their respective controls (**Figure 2C; Supplemental Figure 6**). Indeed, while NLRP3 protein was detectable in 8/9 MCT-RVs, only 4/8 PAB-RVs, 2 sham and 2 PBS-RVs had detectable NLRP3. Pro-CASP1 and pro-IL1β were detected in PAB and MCT RVs; however, increased expression of cleaved-CASP1 and IL1β, which indicates activation of the

AJRCCM Articles in Press. Published June 14, 2022 as 10.1164/rccm.202110-2274OC

inflammasome, were only observed in MCT-RVs (*p=0.031* and *p=0.028*, respectively) (**Figure 2C; Supplemental Figure 6)**. In SuHx rats, the activation of the NLRP3 inflammasome pathway was determined by quantifying cleaved- GSDMD, a protein cleaved by CASP1 and participates in the release of IL1β and pyroptosis.[20]. Cleaved- GSDMD was significantly increased in the SuHX-RVs compared to VeNx (*p=0.002*; **Supplemental Figure 7A**). IL1β was also measured in the serum from SuHx and VeNx rats. Although significant differences were not detected (*p=0.1*; **Supplemental Figure 7B**), there was a trend toward elevated IL1β levels in the serum of SuHx rats.

NLRP3 inflammasome activation was further studied *in vitro* in blood monocytes of MCT *vs.* control rats based on an assay measuring NLRP3:ASC interaction, a key step in inflammasome activation (**Figure 2D**). A time course of inflammasome activation, measured 10-30 minutes after nigericin activation, showed greater NLRP3:ASC interaction 10 minutes after nigericin in MCT *vs.* control monocytes (*p=0.019*; **Figure 2D; Supplemental Figure 8)**. NLRP3 activation *in vitro* was prevented by MCC950 (*p=0.040*; **Figure 2D; Supplemental Figure 8**). These data indicate that increased NLRP3 activation occurs in MCT-monocytes.

SC-144 improved cardiac function, reduced RV-macrophages and suppressed NLRP3 inflammasome and STAT3 activation *in vivo*

GP130 receptor signaling is critical to the proliferation and recruitment of macrophages. It complexes with different members of the IL6 receptor family, allowing the binding of cytokines and the activation of transcription factors such as STAT3. Therefore, we tested whether SC-144, a GP130 inhibitor, would improve RV function by reducing the influx of macrophages to RV, and consequently preventing NLRP3 inflammasome activation. GP130 antagonist-treated MCT rats (MCT-GP130Antag) showed a significant reduction in RVH compared to vehicle-treated rats

AJRCCM Articles in Press. Published June 14, 2022 as 10.1164/rccm.202110-2274OC

(MCT-V). MCT-GP130Antaganist rats also had increased TAPSE (*p=0.004*) and CO (*p=0.030*), and reduced RVFWT (*p=0.0001*; **Figure 3A)**. Ventricular-to-arterial coupling was also improved by SC-144, as assessed by measuring the ratio of RV end-systolic elastance (Ees) to effective arterial elastance (Ea) **(Figure 3A)**. Hypertrophy of RV-cardiomyocytes in the MCT-GP130Antag group was also reduced (*p<0.0001*; **Figure 3B**). This improvement in RV function occurred independently of changes in the severity of pulmonary hypertension, as measured by PAAT, Ea, RVSP (**Figure 3A;** pressure-volume loops are demonstrated in **Supplemental Figure 2B)**, or the severity of adverse pulmonary vascular remodeling, as measured by pulmonary arterial medial thickness **(Figure 3C**). A reduction in RV collagen deposition (*p=0.018*; **Figure 3D**), macrophage accumulation (*p=0.008*; **Figure 3E**), and phosphorylation of STAT3 in macrophages (*p=0.049*; **Figure 3F**) was also observed with SC-144 treatment. Furthermore, SC-144 treatment reduced the NLRP3 and pro-CASP1 protein content in the MCT-RV (*p= 0.028* and *p= 0.028*, respectively; **Figure 3G).** Cleaved forms of CASP1 or IL1B were not detected.

In vivo* treatment with MCC950 inhibits NLRP3 inflammasome activation and improves RV function in the MCT-rats while reducing monocyte-driven hypertrophy and mitochondrial damage in normal cardiomyocytes *in vitro

MCC950 significantly improved RV function in MCT (MCT-MCC950) compared to vehicle-treated (MCT-V) rats (**Figure 4A**), evident as improved TAPSE (*p=0.004*), and CO (*p=0.0208)* MCC950 also improved ventricular-to-arterial coupling (TAPSE to RVSP ratio; *p*=0.0146)[21] and PAAT (*p=0.010*) while reducing RVSP (*p=0.042*) and pulmonary arterial medial wall thickness (*p<0.0001*; **Figure 4A and B).** The Fulton Index improved in all except 3 rats (3/11), creating a trend toward reduction in RVH (*p=0.076*, **Figure 4A**). RV-NLRP3 and cleaved-IL1β

AJRCCM Articles in Press. Published June 14, 2022 as 10.1164/rccm.202110-2274OC

content were significantly reduced in MCT-MCC950 *vs.* MCT-V rats (*p=0.035*, and *p=0.0082*, respectively; **Figure 4C)**. Although MCC950 did not alter RV-collagen deposition (*p=0.161* using a non-parametric test; **Figure 4D**), it shows a clear trend in reducing it. MCC950 also did not reduce RV macrophage count (*p=0.843*; **Figure 4E**).

To assess the specific effects of the *in vivo* MCC950 treatment on NLRP3 inflammasome inhibition on monocytes (which are precursors of macrophages in the bloodstream) and amelioration of cardiomyocyte function, we treated MCT rats with MCC950 and co-cultured their enriched monocytes with healthy neonatal cardiomyocytes (**Supplemental Figure 9**). Compared to control-monocytes, MCT-monocytes significantly reduced the number of cardiomyocytes in culture (after 48 hours *p=0.019*), induced myocyte hypertrophy (24- and 48-hours *p<0.0001;* **Figure 4F**), while causing mitochondrial dysfunction, evidenced by reduced membrane potential (*p=0.005*), and increased mitochondrial fragmentation (increased punctate morphology *p<0.0001 vs.* decreased filamentous morphology; *p<0.0001*), as measured by machine learning[22] (**Figure 4G** and **Supplemental Figure 10**). Conversely, cardiomyocytes co-cultured with monocytes enriched from MCT rats treated *in vivo* with MCC950 restored cardiomyocyte number (*p=0.0003*), reduced myocyte hypertrophy (*p<0.0001*), preserved mitochondrial membrane potential (*p=0.045*) and reduced mitochondrial fragmentation (*p=0.0007*). Interestingly, when monocytes (from PBS, MCT or MCT-MCC950 rats) were stimulated *in vitro* with nigericin (a potent NLRP3 inflammasome activator) prior to the co-culture, no cardiomyocytes grew (data not shown since no cells survived). In these experiments, the cardiomyocytes that were co-cultured with monocytes were never exposed to MCC950.

AJRCCM Articles in Press. Published June 14, 2022 as 10.1164/rccm.202110-2274OC

RV-macrophage numbers are increased, and the NLRP3 inflammasome is activated in the decompensated RV from PAH patients

Patient information is summarized in **Table 1**. Fibrosis and $CD68^+$ macrophage numbers were significantly increased in the RV tissue of PAH patients with decompensated RVs compared to control patients (*p=0.002*; *p=0.029* respectively; **Figure 5A and B**). Although we could not detect differences in the number of $CD68^+NLRP3^+$ cells by immunofluorescence between patients *vs.* controls (**Figure 5C**), immunoblotting showed that the expression of pro and cleaved IL1β were higher in PAH-RV tissue compared to control RVs (*p=0.012* and *p=0.040*, respectively; **Figure 5D**). Using immunofluorescence, we did not detect significant changes in the numbers of macrophages expressing p-STAT3 or GP130 ($CD68^+GP130^+$p-$STAT3^+$, $CD68^+GP130^+$p-$STAT3^-$, $CD68^+GP130^-$p-$STAT3^+$) between PAH and control patients (**Figure 5E**).

M2-like polarization of lung macrophages in MCT rats

To confirm the unique PAH-RV-macrophage phenotype, we conducted a concomitant investigation of lung macrophage phenotype, in MCT and PAB rats. As expected, lung macrophages were more abundant in MCT rats than in controls (MCT 3-weeks; *p=0.033*) (**Figure 6A**). In contrast to RV-macrophages, we detected a shift towards M2-like macrophages in the lungs of MCT rats, characterized by increased expression of ARG1 *(p=0.002)* and CD163 *(p=0.039)* and a decreased incidence of $NOS2^+$ inflammatory macrophages *(p=0.014* in MCT 3-weeks; **Figure 6B***)*. When polarization was assessed in blood monocytes, we detected a significant increase in both anti-inflammatory and inflammatory monocyte subsets after MCT treatment: $CD43^{high}$ (which are anti-inflammatory; *p=0.004*) and $CD43^{low}$ (which are inflammatory; *p=0.021*)[23] (**Figure 6C**).

AJRCCM Articles in Press. Published June 14, 2022 as 10.1164/rccm.202110-2274OC

Discussion

PAH leads to death in approximately half of the patients within 5-years due to RVF[24], and all approved therapies are vasodilators that primarily target the pulmonary vasculature[24,25]. In this study, we considered the possibility that the PAH-RV might be a primary target for inflammation-mediated dysfunction and not just a bystander organ responding to an increase in RV afterload. We compared two preclinical rat models of decompensated RVH (MCT and the SuHx models)[26-27], to the pulmonary artery banding (PAB) model, in which (at the severity of banding we used) the RV retains a compensated RVH phenotype[16,28], mimicking pulmonic stenosis. We also compared RV samples of PAH patients with decompensated RVF to control subjects who had cardiac diseases other than PAH (**Table 1**).

We show in the MCT and SuHx models that RV infiltration with monocyte-derived macrophages and NLRP3 inflammasome activation creates a state of inflammation that contributes to RVF. This is relevant to patients with PAH since we demonstrate that key aspects of the macrophage-NLRP3 inflammasome pathway are similarly deranged in PAH patients with decompensated RVF. Our data confirm that macrophages are the most frequent leukocytes in the PAH-RV (constituting over 45% of $CD45^+$ cells in MCT rats), and they highly express NLRP3. Notably, over 50% of cells in the RV expressing CCR2, a chemotaxis receptor present in inflammatory cells[27], were macrophages in both PAH models. Thus, not only the macrophage numbers are increased in the RV in PAH, but most macrophages in the pulmonary hypertensive RV are derived from blood monocytes. Moreover, there was no macrophage accumulation in the LV in PAH, suggesting the inflammatory infiltration of the RV is a chamber-specific phenomenon in PAH.

AJRCCM Articles in Press. Published June 14, 2022 as 10.1164/rccm.202110-2274OC

To establish the pathological contribution of macrophage infiltration to RV fibrosis and RVF in PAH, we assessed the therapeutic effect of two unrelated agents that target the NLRP3 pathway in MCT rats *in vivo*: SC-144, a GP130 inhibitor (a signal-transducing component of the IL6 cytokine superfamily; IL6ST)[29] and MCC950, a specific inhibitor of the NLRP3 inflammasome[30]. Both of these therapies substantially improved RV function when administered *in vivo,* indicating that therapeutic modulation of the NLRP3-macrophage pathway may be a mechanism to augment RV function in PAH.

Important markers of RV dysfunction (ANP) and fibrosis (total collagen and collagen-III) were elevated in the MCT and SuHx models of maladaptive RVH but not in the PAB model (adaptive). In a previous study, we demonstrated that RV fibroblasts isolated from MCT rats are epigenetically and metabolically reprogrammed to a hyperproliferative and fibrogenic phenotype[4,24]. Therefore, we considered that the RV fibrosis in the MCT model might contribute to a decompensated RV response, which could be triggered by inflammation. As predicted, both drugs that inhibited the inflammasome reduced RV fibrosis (**Figures 3D and 4D**). Although increased RVSP and RVH occurred in all models, only MCT and SuHx rats suffered from RVF

Unlike PAB rats, MCT and SuHx rats had increased numbers of RV-macrophages and evidence of increased NLRP3 inflammasome expression and activation. The macrophage-NLRP3 pathway was not activated in PAB-RVs, indicating that RV pressure overload or RVH alone, at the severity we achieved, does not trigger inflammation. A comparison between rats at 3- and 4-weeks after MCT treatment further confirmed progressive RV decompensation of the MCT model at week 4, evident by worsening of RV function and higher recruitment of macrophages compared to rats euthanized at week 3. Comparing the RV and LV, only MCT- and SuHx-RVs showed higher collagen-III, ANP and macrophage count. These data confirm that the inflammatory and

AJRCCM Articles in Press. Published June 14, 2022 as 10.1164/rccm.202110-2274OC

fibrotic changes in experimental PAH are chamber-specific and not due to any systemic inflammatory effects of any model. We showed that the inhibition of both macrophage recruitment (achieved by SC-144) and NLRP3 inflammasome activation (MCC950) ameliorates fibrosis and improves RV function. Human RV samples also showed augmented fibrosis and increased macrophages in decompensated PAH-RVF patients. The NLRP3 inflammasome pathway was also activated in the RVs of PAH patients, evident as increased expression of both pro-and cleaved-IL1β. However, we failed to detect an increase in NLRP3 protein, which may be a function of sample size and potential variability in the antigen retrieval of this protein in bio-banked, human, histological specimens.

The priming and activation of the NLRP3 inflammasome in macrophages may result from multiple signals such as DAMPs, K^+ efflux, Ca^{2+} influx, and mitochondrial dysfunction[13,31,32]. Disturbances in these signals are well described in PAH[33], supporting the idea that the RV tissue is a fertile environment for the activation of this inflammatory pathway. Indeed, our results demonstrated that the co-culture of healthy cardiomyocytes with monocytes isolated from MCT rats (which have an activated NLRP3 inflammasome) developed cardiotoxicity evidenced by impaired growth, lower mitochondrial membrane potential and increased mitochondrial fragmentation. Once activated, NLRP3 recruits ASC and pro-CASP1, resulting in CASP1 activation and the cleavage of IL1β to its mature form[19]. Therefore, our data suggest that RV inflammation in PAH is maintained by a vicious cycle of cardiomyocyte mitochondrial damage, with production of DAMPs and the release of cleaved- IL1β by macrophages, which is known to mediate cardiomyocyte apoptosis[34].

In PAH patients, IL1β is elevated in the serum[35], and is associated with an increased risk of death[8]. Consistent with this observation, we show for the first time that IL1β is upregulated in

AJRCCM Articles in Press. Published June 14, 2022 as 10.1164/rccm.202110-2274OC

the RV of both MCT rats and patients with decompensated RVF. Higher serum levels of IL1β were also reported in PAH patients carrying somatic mutations in ten-eleven translocation methylcytosine dioxygenase (TET2) compared to non-carrier PAH patients[5,36]. TET2 is a critical regulator of DNA methylation predominantly expressed in monocytic (monocytes and macrophages) and granulocytic cell lineages. Indeed, a hematopoietic-specific knockout of TET2 was sufficient to cause an inflammatory mouse model of PAH, which was reversed by canakinumab, an IL1β antibody[6]. In the current study, we used MCC950, which binds to NLRP3 and inhibits ASC oligomerization[37]. MCC950 remarkably reduced NLRP3 expression and cleaved- IL1β content in the MCT-RV while improving cardiac function without changing the number of RV-macrophages. This was expected since MCC950 blocks the interaction between NLRP3 and ASC and prevents the cleavage of IL1β. Indeed, the cardioprotective benefits of blocking the NLRP3 inflammasome, specifically in monocytes, were seen when monocytes from MCT rats treated *in vivo* with MCC950 were co-cultured with healthy cardiomyocytes. In contrast to MCT-monocytes, which induced hypertrophy, growth restriction and mitochondria dysfunction, the effects of MCT-MCC950- monocytes on cardiomyocytes were comparable to PBS-monocytes. These data are consistent with monocyte-derived RV macrophages being the effector cell in which NLRP3 activation, relevant to cardiotoxicity in RVF, occurs. Consistent with this hypothesis, previous work shows NLRP3 knockout mice exposed to hypoxia have less RV hypertrophy than control mice despite having the same severity of PH[38]. Taken together, these data indicate that MCC950 may have therapeutic potential in the treatment of inflammatory RVF[34, 39, 40].

We investigated the polarization of macrophages in MCT rats by measuring the expression of M1-like (NOS2) and M2-like (CD163 and ARG1) macrophage markers. While lung macrophages acquired an M2-like phenotype (high expression of CD163 and ARG1 and low

AJRCCM Articles in Press. Published June 14, 2022 as 10.1164/rccm.202110-2274OC

NOS2 expression), the RV-macrophages had no change in ARG1, strongly suggesting a unique pattern in the activation of RV-macrophages favoring an inflammatory, M1 phenotype in PAH RV. We also demonstrated that p-STAT3^{+} macrophages are more abundant in the MCT-RVs compared to control. IL6 signaling and STAT3 activation are essential in the proliferation and differentiation of monocytes and macrophages[41]. IL6 is upregulated in the serum of PAH patients[42] and this is directly associated with RVF. Moreover, overexpression of IL6 in murine models leads to the development of pulmonary vascular lesions and PAH[43]. On the other hand, STAT3 is also linked to the activation of M2-like macrophages through IL6 signaling[44] and the regulation of ARG1-expressing alveolar macrophages in hypoxia-induced PH in mice[45]. Thus, while in lung macrophages, the activation of STAT3 may lead to anti-inflammatory polarization, its activation in the RV may be linked to the recruitment and differentiation of monocytes into inflammatory macrophages. Of note, both subsets of monocytes, inflammatory (CD43^{low}) and anti-inflammatory (CD43^{high}), were increased in the blood of MCT rats, supporting the potential for heterogeneous recruitment of cells with different inflammatory profiles to the RV *vs.* the lung.

Our findings using the SC-144 in MCT rats also reinforce the importance of IL6 signaling in recruiting monocyte-derived macrophages to the RV. SC-144 reduced RV-macrophages in MCT rats and diminished the RV's NLRP3 and pro-CASP1 content. These data suggest that reducing the incidence of RV-macrophages, which are the main site of NLRP3 inflammasomes complex activation, can prevent the accumulation of these inflammasome components in the RV tissue. SC-144 also reduced fibrosis and improved RV function independent of the regression of pulmonary vascular obstruction, indicating that the benefits of blocking IL6 signaling are RV-specific. Similar findings were recently reported by Prisco et al.[46]. Although a delay in pulmonary vascular disease was shown by Tamura et al. when rats were treated with IL6R/sIL6R antagonist

AJRCCM Articles in Press. Published June 14, 2022 as 10.1164/rccm.202110-2274OC

(TB-2-081), only a slight improvement in mPAP was reported despite a significant reduction in total pulmonary resistance (TPR), the ratio of mPAP/ CO[47]. This suggests that the decrease in TPR was mainly due to improved CO rather than positive pulmonary vascular remodeling[47]. It is noteworthy that the drug was given one week after MCT injection to Wister rats, a week earlier than given in our study, which might increase its opportunity to improve PAH by preventing (rather than regressing) adverse pulmonary vascular remodeling. Toshner et al. reported that tocilizumab (an IL-6 specific antibody) did not significantly alter PAH severity in human PAH[48]. On the other hand, a study showed that Cardiotrophin-1, a member of the IL6 superfamily of cytokines that activates the GP130 receptor (i.e. an agonist of this pathway), is protective against pulmonary vascular remodeling in hypoxic PH[49], making it unlikely that a GP130 antagonist would cause beneficial pulmonary vascular remodeling. These data align with our findings that SC-144 selectively improved RV function without improving pulmonary vascular remodeling. In another study, SC-144 was used at a different dose, and although the authors reported that the drug regressed pulmonary vascular disease, the representative images of their histological findings showed larger-sized pulmonary arteries than the ones usually used to measure pulmonary medial wall thickness, making data comparison between our studies difficult[50].

Our work suggests a critical role of RV inflammation in controlling adverse RV remodeling and dysfunction in PAH. Still, this study has important ***limitations.*** First, we acknowledge the lack of assessment of sex differences in the role of NLRP3 in PAH. Second, the relatively small sample size for the human study and the lack of lung tissue prevented us from contrasting macrophage polarity or NLRP3 inflammasome activation in the patient's lung *vs.* the heart. Third, although we show mitochondrial damage in cardiomyocytes can occur in the presence of MCT monocytes, we did not establish which DAMPs activate the NLRP3 inflammasome in

AJRCCM Articles in Press. Published June 14, 2022 as 10.1164/rccm.202110-2274OC

PAH-RVs. Fourth, we only used three markers to determine the polarization of RV and lung macrophages in rats, a weakness that affects this field of research since there is a paucity of well-characterized markers to define macrophage polarization in rats (unlike mice, for which there are abundant markers). Finally, the numbers of p-STAT3^{+} macrophages in human PAH-RV tissue did not differ from controls. While this difference may be related to tissue handling or the terminal stage of disease in which these patients were studied, disparities between species in the cell signaling could be at play, and this merits future investigation.

In conclusion, the activation of the NLRP3 inflammasome pathway within the RV-macrophages is present in two robust preclinical models of PAH and in patients with decompensated RVH. *In vivo,* blockade of the IL6 cytokine pathway via SC-144, or the NLRP3 inflammasome signaling, via MCC950 prevented RV-macrophage accumulation and NLRP3 inflammasome activation while improving RV function. These findings indicate that NLRP3 activation contributes to the pathogenesis of RVF. Moreover, our research suggests that RVF is chamber-specific and can occur due to macrophage-mediated inflammation rather than simply being reflective of a failure to adapt to increased RV afterload. Additional research will be required to determine the translational value of GP130 antagonists and MCC950 as potential PAH therapies in humans.

Acknowledgments: We would like to thank Sandra Breuils-Bonnet for her assistance in collecting human hemodynamic data. We also appreciate the support we received from Queen's Cardiopulmonary Unit (QCPU).

Tables:

Table 1: Patient clinical information

	Male		*p*-value	Female		*p*-value
	Control	†Decomp-RVF		Control	Decomp-RVF	
Cardiac Ultrasound						
‡ NT-proBNP (pg/ml)	**68.57 ± 82.25 (14/15)**	**5583.4 ± 7202.61 (5/5)**	**0.006****	**113.63 ± 47.88 (8/8)**	**7472 ± 5837.31 (8/9)**	**0.004****
§TAPSE (mm)	**22.2 ± 2.68 (10/15)**	**13.8 ± 5.98 (5/5)**	**0.004****	**20 ± 4.40 (6/8)**	**15.8 ± 6.30 (8/9)**	**0.091**
Cardiac output (L/min)	**5.01 ± 1.03 (7/15)**	**3.94 ± 0.49 (5/5)**	**0.071**	**7.1 ± 1.10 (2/8)**	**4.1 ± 0.94 (8/9)**	**0.008****
Cardiac index (L/min/m2)	**2.86 ± 0.47 (4/15)**	**1.99 ± 0.60 (5/5)**	**0.878**	**3.28 ± 0.28 (2/8)**	**2.35 ± 0.57 (8/9)**	**0.078**
White blood cells count						
Total WBC ($x10^9$/litre)	**9.61 ± 6.67**	**8.06 ± 1.36**	**0.620**	**6.57 ± 1.25**	**14.21 ± 6.30**	**0.038***
Neutrophils ($x10^9$/litre)	**7.05 ± 6.67**	**5.74 ± 1.52**	**0.640**	**4.12 ± 0.70**	**12.12 ± 5.74**	**0.022***
Monocytes $x10^9$/litre	**0.61± 0.43**	**0.64±0.39**	**0.890**	**0.57±0.17**	**0.55±0.31**	**0.891**

Values are presented as Mean ± SEM. Student's t-test Males (Control *vs* Decomp-RVF) vs Female (Control *vs* Decomp-RVF): *(p≤0.05), **(p≤0.01), *(p≤0.001), and ****(p≤0.0001)**
† Decomp-RVF= decompensated Right Ventricular Failure, ‡ NT-proBN*P* = N-terminal pro-b-type natriuretic peptide.
§ TAPSE= Tricuspid Annular Plane Systolic Excursion
Total number of subjects n=37: male control 15, male decomp-RVF 5, female control 8, female decomp-RVF 9
Values in between brackets represent the number of subjects that have the parameter calculated. The female and male control groups were diagnosed with cardiomyopathies other than PAH.

AJRCCM Articles in Press. Published June 14, 2022 as 10.1164/rccm.202110-2274OC

Table 2: Rat cardiac function information

	MCT-model			SuHx-model			PAB-model		
	PBS	MCT- 4 weeks	*p*-value	VeNx	SuHx	*p*-value	Sham	PAB	*p*-value
Cardiac Ultrasound									
†RVFWT–dias (mm)	0.64±0.024	1.36±0.166	0.0006***	-	-	-	0.63±0.024	1.04±0.099	0.0003***
TAPSE	2.88 ± 0.094	1.76±0.130	0.0012**	-	-	-	2.62±0.120	2.97±0.200	0.155
‡CO (mL/min)	122.40±5.195	56.57±5.879	0.0006***	-	-	-	-	-	-
§PAAT (ms)	31.71±1.409	20.01±1.492	0.0012**	-	-	-	-	-	-
RHC									
††RVSP (mmHg)	22.69±1.022	51.32 ±2.510	0.0007***	24.83± 4.02	48.80±6.45	0.0043**	21.10 ± 1.576	61.70±7.058	0.0012**
RVEDP	0.946±0.304	4.851±0.568	0.0007***	2.01±0.43	3.98±0.36	0.0159*	1.036±0.162	2.138±0.17	0.007**
EF	78.66±1.721	51.19±4.914	0.0007***	70.73±4.91	59.22±2.5	0.0036**	75.66±5.98	72.15±4.16	0.640
CO (mL/min)	139.1 ± 4.120	54.38±9.33	0.0006***	113.8±12.15	84.23±13.76	0.0159*	125.0±17.2	120.1±19.06	0.249
§§CI	0.334±0.088	0.207±0.025	0.025*	0.1980±0.03	0.1825±0.02	0.45	0.300±0.02	0.323±0.038	0.218
Anatomical parameter									
Fulton Index	0.213 ± 0.014	0.311 ± 0.041	0.004**	0.266±0.02	0.448±0.06	0.0043**	0.227±0.023	0.374±0.093	0.022*

Values are presented as Mean± SEM.
Non-parametric T-test (Mann- Whitney) was used to compare MCT, SuHx and PAB rats with their respective controls: *(p≤0.05), **(p≤0.01), *(p≤0.001).**
†RVFWT– dias= Right ventricular free wall thickness in diastole, ‡CO= cardiac output, § PAAT= pulmonary artery acceleration time, ††RVS*P* =*R*ight ventricular systolic pressure, §§CI= cardiac index
PBS n=6, MCT n=8, VeNx n=6, SuHx n=5, Sham n=5, PAB n=5

AJRCCM Articles in Press. Published June 14, 2022 as 10.1164/rccm.202110-2274OC

References:

1. Simonneau G, Hoeper MM. The revised definition of pulmonary hypertension: Exploring the impact on patient management. *Eur Hear Journal, Suppl*. 2019;21(Suppl K):K4-K8. doi:10.1093/eurheartj/suz211
2. Vonk-Noordegraaf A, Haddad F, Chin KM, et al. Right heart adaptation to pulmonary arterial hypertension: Physiology and pathobiology. In: *Journal of the American College of Cardiology*. ; 2013. doi:10.1016/j.jacc.2013.10.027
3. Ryan JJ, Huston J, Kutty S, et al. Right ventricular adaptation and failure in pulmonary arterial hypertension. *Can J Cardiol*. 2015;31(4):391-406. doi:10.1016/j.cjca.2015.01.023
4. Tian L, Wu D, Dasgupta A, et al. Epigenetic Metabolic Reprogramming of Right Ventricular Fibroblasts in Pulmonary Arterial Hypertension: A Pyruvate Dehydrogenase Kinase-Dependent Shift in Mitochondrial Metabolism Promotes Right Ventricular Fibrosis. *Circ Res*. 2020;126(12):1723-1745. doi:10.1161/CIRCRESAHA.120.316443
5. Potus F, Pauciulo MW, Cook EK, et al. Novel mutations and decreased expression of the epigenetic regulator TET2 in pulmonary arterial hypertension. *Circulation*. 2020;141(24):1986-2000. doi:10.1161/CIRCULATIONAHA.119.044320
6. Savai R, Pullamsetti SS, Kolbe J, et al. Immune and inflammatory cell involvement in the pathology of idiopathic pulmonary arterial hypertension. *Am J Respir Crit Care Med*. 2012;186(9):897-908. doi:10.1164/rccm.201202-0335OC
7. Humbert M, Monti G, Brenot F, et al. Increased interleukin-1 and interleukin-6 serum concentrations in severe primary pulmonary hypertension. *Am J Respir Crit Care Med*. 1995;151(5):1628-1631. doi:10.1164/ajrccm.151.5.7735624
8. Cracowski JL, Chabot F, Labarère J, et al. Proinflammatory cytokine levels are linked to

AJRCCM Articles in Press. Published June 14, 2022 as 10.1164/rccm.202110-2274OC

death in pulmonary arterial hypertension. *Eur Respir J*. 2014;43(3):915-917. doi:10.1183/09031936.00151313

9. Florentin J, Coppin E, Vasamsetti SB, et al. Inflammatory Macrophage Expansion in Pulmonary Hypertension Depends upon Mobilization of Blood-Borne Monocytes. *J Immunol*. 2018;200(10):3612-3625. doi:10.4049/jimmunol.1701287
10. Mosser DM, Edwards JP. Exploring the full spectrum of macrophage activation. *Nat Rev Immunol*. 2008;8(12):958-969. doi:10.1038/nri2448
11. Zhou R, Yazdi AS, Menu P, Tschopp J. A role for mitochondria in NLRP3 inflammasome activation. *Nature*. 2011;469(7329):221-226. doi:10.1038/nature09663
12. Swanson K V., Deng M, Ting JPY. The NLRP3 inflammasome: molecular activation and regulation to therapeutics. *Nat Rev Immunol*. 2019;19(8):477-489. doi:10.1038/s41577-019-0165-0
13. Kelley N, Jeltema D, Duan Y, He Y. The NLRP3 Inflammasome: An Overview of Mechanisms of Activation and Regulation. *Int J Mol Sci*. 2019;20(13):3328. doi:10.3390/ijms20133328
14. Al-Qazazi R, Lima PD, Potus F, et al. Increased Right Ventricular Macrophages and NLRP3 in Monocrotaline Pulmonary Hypertension. *Circulation*. 2019;140(Suppl_1):A15947. doi:10.1161/circ.140.suppl_1.15947
15. Lima PD, Al-Qazazi R, Prisco SZ, et al. NLRP3 Inflammasome Activation in Macrophages Drives Adverse Right Ventricular Remodeling and Dysfunction. *Circulation*. 2021;144(Suppl_1):A13924. doi:10.1161/circ.144.suppl_1.13924
16. Andersen S, Schultz JG, Holmboe S, et al. A pulmonary trunk banding model of pressure overload induced right ventricular hypertrophy and failure. *J Vis Exp*.

AJRCCM Articles in Press. Published June 14, 2022 as 10.1164/rccm.202110-2274OC

2018;2018(141):e58050. doi:10.3791/58050

17. Tian L, Potus F, Wu D, et al. Increased Drp1-mediated mitochondrial fission promotes proliferation and collagen production by right ventricular fibroblasts in experimental pulmonary arterial hypertension. *Front Physiol*. 2018;9(JUL). doi:10.3389/fphys.2018.00828
18. Van Hout GPJ, Bosch L, Ellenbroek GHJM, et al. The selective NLRP3-inflammasome inhibitor MCC950 reduces infarct size and preserves cardiac function in a pig model of myocardial infarction. *Eur Heart J*. 2017;38(11):828-836. doi:10.1093/eurheartj/ehw247
19. Provencher JF, Borrelle SB, Bond AL, et al. Recommended best practices for plastic and litter ingestion studies in marine birds: Collection, processing, and reporting. *Facets*. 2019;4(1):111-130. doi:10.1139/facets-2018-0043
20. He WT, Wan H, Hu L, et al. Gasdermin D is an executor of pyroptosis and required for interleukin-1β secretion. *Cell Res 2015 2512*. 2015;25(12):1285-1298. doi:10.1038/cr.2015.139
21. Tian L, Xiong PY, Alizadeh E, et al. Supra-coronary aortic banding improves right ventricular function in experimental pulmonary arterial hypertension in rats by increasing systolic right coronary artery perfusion. *Acta Physiol*. 2020;229(4). doi:10.1111/apha.13483
22. Wu D, Dasgupta A, Chen KH, et al. Identification of novel dynamin-related protein 1 (Drp1) GTPase inhibitors: Therapeutic potential of Drpitor1 and Drpitor1a in cancer and cardiac ischemia-reperfusion injury. *FASEB J*. 2020;34(1):1447-1464. doi:10.1096/FJ.201901467R
23. Yrlid U, Milling SWF, Miller JL, Cartland S, Jenkins CD, MacPherson GG. Regulation of

AJRCCM Articles in Press. Published June 14, 2022 as 10.1164/rccm.202110-2274OC

Intestinal Dendritic Cell Migration and Activation by Plasmacytoid Dendritic Cells, TNF-α and Type 1 IFNs after Feeding a TLR7/8 Ligand. *J Immunol*. 2006;176(9):5205-5212. doi:10.4049/jimmunol.176.9.5205

24. Thenappan T, Ormiston ML, Ryan JJ, Archer SL. Pulmonary arterial hypertension: Pathogenesis and clinical management. *BMJ*. 2018;360. doi:10.1136/bmj.j5492

25. Prisco SZ, Thenappan T, Prins KW. Treatment Targets for Right Ventricular Dysfunction in Pulmonary Arterial Hypertension. *JACC Basic to Transl Sci*. 2020;5(12):1244-1260. doi:10.1016/J.JACBTS.2020.07.011

26. Rabinovitch M. Monocrotaline-Induced Pulmonary Hypertension in Rats. 2001:261-280. doi:10.1007/978-1-59259-003-2_19

27. Dahal BK, Kosanovic D, Kaulen C, et al. Involvement of mast cells in monocrotaline-induced pulmonary hypertension in rats. *Respir Res*. 2011;12(1):60. doi:10.1186/1465-9921-12-60

28. Ryan JJ, Archer SL. The right ventricle in pulmonary arterial hypertension: disorders of metabolism, angiogenesis and adrenergic signaling in right ventricular failure. *Circ Res*. 2014;115(1):176-188. doi:10.1161/CIRCRESAHA.113.301129

29. West NR. Coordination of immune-stroma crosstalk by IL-6 family cytokines. *Front Immunol*. 2019;10(MAY):1093. doi:10.3389/fimmu.2019.01093

30. Van Hout GPJ, Bosch L, Ellenbroek GHJM, et al. The selective NLRP3-inflammasome inhibitor MCC950 reduces infarct size and preserves cardiac function in a pig model of myocardial infarction. *Eur Heart J*. 2017;38(11):828-836. doi:10.1093/eurheartj/ehw247

31. Seok JK, Kang HC, Cho YY, Lee HS, Lee JY. Therapeutic regulation of the NLRP3 inflammasome in chronic inflammatory diseases. *Arch Pharm Res*. 2021;44(1):16-35.

AJRCCM Articles in Press. Published June 14, 2022 as 10.1164/rccm.202110-2274OC

doi:10.1007/s12272-021-01307-9

32. Yuan X-J, Wang J, Juhaszova M, Gaine SP, Rubin LJ. Attenuated K+ channel gene transcription in primary pulmonary hypertension. *Lancet*. 1998;351(9104):726-727. doi:10.1016/S0140-6736(05)78495-6

33. Dasgupta A, Wu D, Tian L, et al. Mitochondria in the Pulmonary Vasculature in Health and Disease: Oxygen-Sensing, Metabolism, and Dynamics. In: *Comprehensive Physiology*. Vol 10. Wiley; 2020:713-765. doi:10.1002/cphy.c190027

34. Shen Y, Qin J, Bu P. Pathways Involved in Interleukin-1β–Mediated Murine Cardiomyocyte Apoptosis. *Texas Hear Inst J*. 2015;42(2):109. doi:10.14503/THIJ-14-4254

35. Soon E, Holmes AM, Treacy CM, et al. Elevated levels of inflammatory cytokines predict survival in idiopathic and familial pulmonary arterial hypertension. *Circulation*. 2010;122(9):920-927. doi:10.1161/CIRCULATIONAHA.109.933762

36. Cull AH, Snetsinger B, Buckstein R, Wells RA, Rauh MJ. Tet2 restrains inflammatory gene expression in macrophages. *Exp Hematol*. 2017;55:56-70.e13. doi:10.1016/j.exphem.2017.08.001

37. Jiang M, Li R, Lyu J, et al. MCC950, a selective NLPR3 inflammasome inhibitor, improves neurologic function and survival after cardiac arrest and resuscitation. *J Neuroinflammation 2020 171*. 2020;17(1):1-12. doi:10.1186/S12974-020-01933-Y

38. Cero FT, Hillestad V, Sjaastad I, et al. Absence of the inflammasome adaptor ASC reduces hypoxia-induced pulmonary hypertension in mice. *Am J Physiol Lung Cell Mol Physiol*. 2015;309(4):L378-L387. doi:10.1152/AJPLUNG.00342.2014

39. Batista AF, Rody T, Forny-Germano L, et al. Interleukin-1β mediates alterations in

AJRCCM Articles in Press. Published June 14, 2022 as 10.1164/rccm.202110-2274OC

mitochondrial fusion/fission proteins and memory impairment induced by amyloid-β oligomers. *J Neuroinflammation*. 2021;18(1):54. doi:10.1186/s12974-021-02099-x

40. Nakayama H, Otsu K. Mitochondrial DNA as an inflammatory mediator in cardiovascular diseases. *Biochem J*. 2018;475(5):839. doi:10.1042/BCJ20170714

41. Nakajima K, Yamanaka Y, Nakae K, et al. A central role for Stat3 in IL-6-induced regulation of growth and differentiation in M1 leukemia cells. *EMBO J*. 1996;15(14):3651. doi:10.1002/j.1460-2075.1996.tb00734.x

42. Prins KW, Archer SL, Pritzker M, et al. Interleukin-6 is independently associated with right ventricular function in pulmonary arterial hypertension. *J Heart Lung Transplant*. 2018;37(3):376-384. doi:10.1016/J.HEALUN.2017.08.011

43. Steiner MK, Syrkina OL, Kolliputi N, Mark EJ, Hales CA, Waxman AB. Interleukin-6 overexpression induces pulmonary hypertension. *Circ Res*. 2009;104(2):236-244. doi:10.1161/CIRCRESAHA.108.182014

44. Mauer J, Chaurasia B, Goldau J, et al. Signaling by IL-6 promotes alternative activation of macrophages to limit endotoxemia and obesity-associated resistance to insulin. *Nat Immunol*. 2014;15(5):423-430. doi:10.1038/ni.2865

45. El Kasmi KC, Pugliese SC, Riddle SR, et al. Adventitial Fibroblasts Induce a Distinct Proinflammatory/Profibrotic Macrophage Phenotype in Pulmonary Hypertension. *J Immunol*. 2014;193(2):597-609. doi:10.4049/jimmunol.1303048

46. Prisco SZ, Hartweck LM, Rose L, et al. Inflammatory Glycoprotein 130 Signaling Links Changes in Microtubules and Junctophilin-2 to Altered Mitochondrial Metabolism and Right Ventricular Contractility. *Circ Heart Fail*. 2022;15(1). doi:10.1161/CIRCHEARTFAILURE.121.008574

AJRCCM Articles in Press. Published June 14, 2022 as 10.1164/rccm.202110-2274OC

47. Tamura Y, Phan C, Tu L, et al. Ectopic upregulation of membrane-bound IL6R drives vascular remodeling in pulmonary arterial hypertension. *J Clin Invest*. 2018;128(5):1956. doi:10.1172/JCI96462

48. Toshner M, Church C, Harbaum L, et al. Mendelian randomisation and experimental medicine approaches to IL-6 as a drug target in PAH. *Eur Respir J*. September 2021:2002463. doi:10.1183/13993003.02463-2020

49. Nomura N, Asano M, Saito T, et al. Cardiotrophin-1 is a prophylactic against the development of chronic hypoxic pulmonary hypertension in rats. *Ann Thorac Surg*. 2003;76(1):237-243. doi:10.1016/S0003-4975(03)00339-4

50. Huang Z, Liu Z, Luo Q, et al. Glycoprotein 130 Inhibitor Ameliorates Monocrotaline-Induced Pulmonary Hypertension in Rats. *Can J Cardiol*. 2016;32(11):1356.e1. doi:10.1016/J.CJCA.2016.02.058

AJRCCM Articles in Press. Published June 14, 2022 as 10.1164/rccm.202110-2274OC

Figure Legends

Figure 1: An increase in RV-macrophages is associated with worsening RV function and increased RV fibrosis in PAH

(A) The mean fluorescence intensity (MFI) of ANP (Alexa-fluor 647; red) was measured per cardiomyocyte via confocal microscopy, and a fold of change analysis shows that it is significantly high in 4-weeks MCT-RV compared to control (n=5/group; *p=0.003).* The fold of change of total collagen deposition (Picrosirius red stain) was higher in the RV of 4-weeks MCT and SuHx (n= 5/group; *p<0.0001*, *p=0.0078*) compared to controls. The total collagen deposition was significantly higher in MCT and SuHx compared to PAB rats (*p<0.0001* and *p=0.008,* respectively). Collagen-III (Alexa-fluor 488; green) expression was higher in 4-weeks MCT-RVs and SuHx RVs compared to controls (n=5/group; *p<0.0001*, *p=0.0078*). PAB-RVs had a significantly lower Collagen-III signal compared to MCT (*p=0.0004*) and SuHx (*p=0.02*) rats. Two-way ANOVA test was used to compare treatment (control *vs.* treated groups) and type of treatment (PAB *vs.* MCT *vs.* SuHx).

(B) *In situ* quantification of macrophages ($CD68^+$ cells) via confocal microscope showed a 5-fold increase in 4-weeks MCT-RVs compared to PBS-RVs (*p<0.0001*). A similar increase in RV-macrophages was observed in SuHx rats (4-fold increase; *p=0.004*), while the number of $CD68^+$ cells in the PAB-RV did not significantly differ from control. The incidence of RV-macrophages in MCT-RVs (*p<0.0001*) and SuHx-RVs (*p=0.0014*) was significantly higher than in PAB-RVs. No significant differences were found when MCT and SuHx were compared regarding the number of RV $CD68^+$ cells.

(C) Quantification of monocyte-derived ($CCR2^+CD68^{+)}$ and tissue-resident ($CCR2^-D68^+$) macrophages in RVs from MCT and SuHx rats. Compared to controls (PBS and VeNx), both

AJRCCM Articles in Press. Published June 14, 2022 as 10.1164/rccm.202110-2274OC

MCT- and SuHx-RVs had a significantly increase in monocyte-derived (MCT *vs.* PBS *p=0.035;* SuHx *vs.* VeNx *p=0.007*) and tissue-resident macrophages (MCT *vs.* PBS *p=0.035;* SuHx *vs.* VeNx *p=0.007).* Monocyte-derived macrophage was the predominant subset in MCT-RVs ($CCR2^+$: 57.77±27.56 *vs.* $CCR2^-$: 33.93±10.66 macrophages per 0.3025mm2), while in SuHx-RVs, monocyte-derived and tissue-resident macrophages had similar incidence $CCR2^+$: 17.40±2.48 *vs.* $CCR2^-$: 22.39±2.74). Two-way ANOVA test was used to compare treatment (control *vs.* treated groups) and type of treatment (PAB *vs.* MCT *vs.* SuHx).

(D) Flow cytometric analysis of live MCT and PAB RV-macrophages ($CD45^+CD68^+$ cells) collected from RV single-cell suspension (PAB, 3-weeks: n=4/group and 4-weeks: n=6/group MCT rats) also confirmed the increase of RV-macrophages in both 3- and 4- weeks MCT rats (*p=0.0286* and *p=0.0022)*, but not in the PAB rats compared to controls. The incidence of macrophages in the RV increased as the MCT-induced disease progressed from 3-weeks to 4-weeks (*p=0.0095*). Two-way ANOVA test was used to compare treatment (control *vs.* treated groups) and type of treatment (3-weeks *vs.* 4-weeks MCT *vs.* PAB).

(E) Correlation analysis of cardiac output and the number of RV-macrophages shows an inverse correlation between the two variables, stronger at week-4 than at week-3 (3-weeks: $r^2=0.293$, $p=0.165$ and 4-weeks: $r^2=0.483$, $p=0.017$).

Figure 2: Increased number of RV macrophages in PAH-rat models is marked by an increase in NLRP3 inflammasome activity

(A) Baseline flow cytometric assessment of NLRP3 content (n= 4 rats) showing higher relative expression of NLRP3 in rat RV-macrophages ($CD45^+CD68^+$) compared to all other cell types,

AJRCCM Articles in Press. Published June 14, 2022 as 10.1164/rccm.202110-2274OC

including: other immune cells ($CD45^+CD68^-$; *p=0.017*), endothelial cells ($CD45^-CD31^+$; *p=0.005*) and fibroblast ($CD45^-CD90^+$; *p=0.008*).

(B) Double immunofluorescence detecting CD68 (Alexa Fluor 555; red) and NLRP3 (Alexa Fluor 488; green) in RV tissue of MCT, SuHx and control rats (PBS and VeNx). The quantification of the relative incidence of $CD68^+NLRP3^+$ cells (Normalized by total $CD68^+$ cells) revealed an increased number of macrophages expressing NLRP3 in the RV of MCT and SuHx rats compared to controls (*p= 0.011, 0.0073*). No differences in the incidence of these cells were found when MCT and SuHx rats were compared.

(C) Western blot analysis (n=8 MCT, 9 PBS, 4 PAB and 4 sham) showed activation of the NLRP3 pathway in MCT but not PAB RVs. NLRP3, cleaved CASP1 and cleaved **IL1β** content were significantly higher in MCT-RVs compared to the control group (*p=0.036*, *0.028*, *p=0.028*, respectively). No significant differences in NLRP3 and cleaved CASP1 were found when comparing PAB-RVs to their controls (sham) (*p=0.281* and *p=0.111* respectively), while cleaved-IL1B was undetectable (red box). The content of target proteins was normalized to vinculin.

(D) *In vitro* culture of blood monocytes isolated from PBMCs of MCT and control rats; (n= 3 rats/group) were challenged with nigericin (10 min) in the presence or absence of MCC950. The NLRP3 and ASC interaction (which indicates inflammasome assembly) was measured using antibodies against NLRP3 (yellow) and ASC (Apoptosis-associated speck-like *protein* containing a CARD) (red) and imaged via super-resolution microscopy. NLRP3:ASC interaction was significantly higher in monocytes from MCT (*p=0.0197*) *vs.* PBS rats after nigericin treatment. MCC950 significantly reduced the NLRP3:ASC interaction (*p=0.0403*). Contra-stain: phalloidin (green) and Dapi (blue).

AJRCCM Articles in Press. Published June 14, 2022 as 10.1164/rccm.202110-2274OC

Figure 3: SC-144 improves cardiac function, reduces RV macrophage number, and suppresses NLRP3 inflammasome and STAT3 activation

(A) GP130 Antagonism improves indicators of RV function in MCT rats when compared to MCT rats treated with vehicle (MCT-V): TAPSE, cardiac output, RVFWT, end-systolic elastance/ effective arterial elastance (*p=0.004*, *0.030*, and *0.0001*, respectively; n= 8-10/ group). While cardiac function was preserved with the GP130 antagonist, there was no difference in Ear, PAAT and RVSP when comparing the MCT-GP130 Antagonist treated group with the MCT-V group.

(B) Histological assessment of RV cardiomyocyte hypertrophy using H&E staining (cardiomyocyte area um^2; n=3 rats/group and >94 cardiomyocytes/rat). GP130 antagonist treatment reversed RV cardiomyocyte hypertrophy in MCT rats (MCT-V *vs*. MCT-Antagonist *p<0.0001*; average area per image;15 images per rat).

(C) Histological Assessment of the median wall thickness of pulmonary arterioles using H&E staining (n=3 rats/group and >20 arterioles/rat). The GP130 antagonist SC-144 failed to ameliorate the arteries' thickness in MCT-rats (Control *vs*. MCT-V *p=0*.013; MCT-V *vs*. MCT-GP130 *p>0*.999).

AJRCCM Articles in Press. Published June 14, 2022 as 10.1164/rccm.202110-2274OC

(D) Fibrosis assessment using Picrosirius staining showed a reduction in the percentage of collagen deposition in an area (n=9 rats/group) in the GP130 antagonist (MCT-GP130 Antagonist) compared to the vehicle group (MCT-V; *p=0.*0183).

(E) Macrophages ($CD68^+$cells per $0.09mm^2$) in the RVs of PBS, MCT-V and MCT-GP130 Antagonist groups were identified using a light microscope (n=9 rats/group). The quantification revealed a significant reduction in the number of $CD68^+$ cells in MCT-RV when the rats were treated with a GP130 antagonist compared to the vehicle control (*p=0.0183*).

(F) Identification and quantification of p-$STAT3^+$ (Alexa Fluor 488; green) and macrophages ($CD68^+$; Alexa Fluor 555; red) using immunofluorescence. The GP130 antagonist treatment significantly decreased the number of p-$STAT3^+CD68^+$ relative to the total number of CD68+ macrophages in MCT rats compared to vehicle control (*p=0.0499*)

(G) Western blot assay showed a significantly lower content of NLRP3 and pro-CASP1 (*p=0.0286* and *0.0571*) in the RVs of MCT rats treated with GP130 antagonist compared to vehicle controls (n=4 rats/group). The content of target proteins was normalized to the intensity of Coomassie Brilliant Blue (CBB; total protein). The cleaved forms of CASP1 and **IL1β** were not detected in this experiment.

Figure 4: MCC950 inhibits NLRP3 inflammasome activation, reduces mitochondrial damage in cardiomyocytes and improves RV function in PAH

(A) The cardiac function in MCC950-treated group, assessed by cardiac ultrasound, was improved in the MCT-MCC950 group compared to MCT-V (n=8 PBS, 8 MCT-V, 11 MCT-MCC950), as demonstrated by increased TAPSE (*p=0.016*), CO (*p=0.042*) and CI (P=0.025). A reduction of the Fulton Index and RVFWT is shown but is not significant (*p=0.076, 0.125*).

AJRCCM Articles in Press. Published June 14, 2022 as 10.1164/rccm.202110-2274OC

Ventricular-to-arterial coupling was also improved and assessed by measuring the ratio of TAPSE to RVSP (*p=0.0146*). There was also a significant improvement in RVSP (*p=0.043*) and PAAT (*p=0.022*).

(B) Histological Assessment of the pulmonary arterioles using H&E staining (n=3 rats/group and >20 arterioles/rat). The percent median wall thickness of the pulmonary arteries was measured, and MCC950 treatment reduced % medial thickness in MCT-rats compared to controls (*p<0.0001* comparing rats or arterioles*).*

(C) Western blot assay showing a significantly lower expression of NLRP3 (*p=0.035*), and cleaved IL1β (*p=0.0082*) in the RVs of MCT rats treated with MCC950 compared to vehicle controls (n=5 PBS, 6 MCT-V and 7 MCT-MCC950 rats). The content of target proteins was normalized with vinculin.

(D) Fibrosis assessment using Picrosirius staining showed a non-significant reduction in collagen deposition (% per image) in the MCC950 group compared to vehicle controls (*p=0.1611*).

(E) Identification and quantification of macrophages ($CD68^+$cells per $0.3025mm^2$) in the RVs of PBS, MCT-V, and MCT-MCC950 groups. No differences were found between MCT-V and MCT-MCC950 treated groups (*p=0.843*), while there was a difference between PBS *vs.* MCT-V (*p=0.0264).*

(F) Assessment of neonatal cardiomyocyte' number and level of hypertrophy when co-cultured with enriched monocytes from PBS, MCT-V and MCT-MCC950. The number of cardiomyocytes co-cultured with MCT monocytes was significantly reduced after 48 hours of co-culture (*p=0.019*), while the cell number in cardiomyocytes co-cultured with MCT-MCC950- derive monocytes were comparable to PBS- derive monocytes (MCT *vs.* MCT-MCC950 *p<0.0001* at 48 hours; PBS *vs.* MCT-MCC950 no significant difference). A significant increase in area was

AJRCCM Articles in Press. Published June 14, 2022 as 10.1164/rccm.202110-2274OC

observed in cardiomyocytes co-cultured with MCT- derived monocytes groups compared to PBS ($p<0.0001$ at 24 hours and $p<0.0001$ at 48 hours) and MCT-MCC950 ($p=0.0026$ at 24 hours and $p<0.0001$ at 48 hours).

(G) Mitochondrial dysfunction was induced in cardiomyocytes co-cultured with MCT-derived monocytes, evidenced by reduced membrane potential (PBS *vs.* MCT $p=0.005$) and pathological mitochondria fragmentation (PBS *vs.* MCT: increased punctate morphology $p<0.0001$; and decreased filamentous morphology $p<0.0001$). These adverse effects were prevented by *in vivo* treatment of rats with MCC950 (MCT *vs.* MCT-MCC950 punctate morphology $p=0.0007$; and filamentous morphology $p<0.013$).

Figure 5: Increased incidence of macrophages and NLRP3 inflammasome activation in the RV from PAH patients with decompensated RVs

(A) Collagen deposition assessment of PAH RV tissue using Picrosirius red staining (n= 8 PAH and 4 controls) demonstrated that PAH RV tissue was significantly richer in collagen compared to control RV tissue ($p=0.002$).

(B) Identification and quantification of human RV-macrophages ($CD68^+$ cells per 0.18 mm^2) showing a significantly higher incidence of macrophages in the PAH group compared to control ($p=0.029$; n=8 PAH and 4 controls).

(C) Identification and quantification of human RV-macrophages expressing NLRP3 ($CD68^+$; red, $NLRP3^+$; green). A non-significant increase in the number of RV-macrophages expressing NLRP3 was detected ($p=0.713$).

(D) Assessment of NLRP3, CASP1 and IL1β content of human PAH-RV using western blot. Pro and cleaved IL1β are significantly increased in PAH-RV compared to control ($p=0.012$ and

AJRCCM Articles in Press. Published June 14, 2022 as 10.1164/rccm.202110-2274OC

p=0.040; n=3/ group). The content of target proteins was normalized using the Ponceau stain (total protein).

(E) Immunofluorescence staining was used to detect p-STAT3 (green), GP130 (yellow) and macrophages (CD68; red). The macrophages subsets: $GP130^{+}$p-$STAT3^{+}CD68^{+}$, $GP130^{+}$p-$STAT3^{-}CD68^{+}$ and $GP130^{-}$p-$STAT3^{+}CD68^{+}$ were quantified, but no subset differences were detected when comparing control and PAH RV tissue.

Figure 6: Distinctive M2 polarization of lung macrophages is consistent with regional heterogeneity in macrophage polarization between the RV and the lung in PAH

(A) Flow cytometric assessment of live lung macrophages ($CD45^{+}CD68^{+}$) of MCT-treated and PAB rats (n=4/group). The incidence of macrophages was at its highest level in the lungs of MCT-treated rats at week 3 after receiving MCT *vs.* PBS controls (a fold of change; *p=0.033*), MCT 4 weeks (*p=0.068*), and PAB rats (*p*=0*.092*). The comparison between 3-weeks and 4 weeks of MCT showed no significant differences. Two-way ANOVA test was used to compare treatment (control *vs.* treated groups) and type of treatment (3-weeks *vs*. 4-weeks MCT).

AJRCCM Articles in Press. Published June 14, 2022 as 10.1164/rccm.202110-2274OC

(B) The polarization of lung macrophages was determined based on the level of expression of ARG1, CD163 (M2-like macrophage markers), and NOS2 (M1-like macrophage marker). There was an increase in the expression of CD163 (*p=0.039*) and ARG1 (*p=0.002*) at 4 weeks after MCT injection, while the percentage of NOS2 expressing macrophages in the MCT-lung was reduced at 3 weeks (*p=0.014).*

(C) Classical ($CD3^{-}/B220^{-}/His48^{lo}/CD43^{hi}$) and non-classical ($CD3^{-}/B220^{-}/His48^{lo}/CD43^{lo}$) blood monocytes incidence were measured using flow cytometry (n= 5/group). MCT significantly increased the incidence of both monocyte subsets (*p=0.004* and *p=0.021*, respectively).

Figure 7: PAH-RVF is triggered by Macrophage-NLRP3 activation and can be targeted by GP130 antagonism or NLRP3 inhibition.

Proposed mechanism of NLRP3 activation in RVF in PAH: proposed mechanism of NLRP3 activation in RVF in PAH: The activation of the NLRP3 inflammasome pathway in RV-macrophages is triggered by mitochondrial dysfunction in cardiomyocytes (source of DAMPs) (1) leading to NLRP3 inflammasome assembling (2) and release of IL1β. IL1β induces RV pro-inflammatory response, including the secretion of other inflammatory cytokines such as IL6 (3). The IL6 downstream signaling via p-STAT3 in monocytes (4) participates in the recruitment of new monocytes/macrophages to the RV (5). The chronic secretion of RV IL1β contributes to mitochondria dysfunction (6), fibrosis and RVF (7). This study proposed two therapeutic approaches to cease the inflammatory process: SC-144, an inhibitor of GP130 (a signal-transducing component of the IL6 cytokine family; therapeutic A) and MCC950 (a specific inhibitor of the NLRP3 inflammasome; therapeutic B).

AJRCCM Articles in Press. Published June 14, 2022 as 10.1164/rccm.202110-2274OC

Figure 1: An increase in RV-macrophages is associated with worsening RV function and increased RV fibrosis in PAH

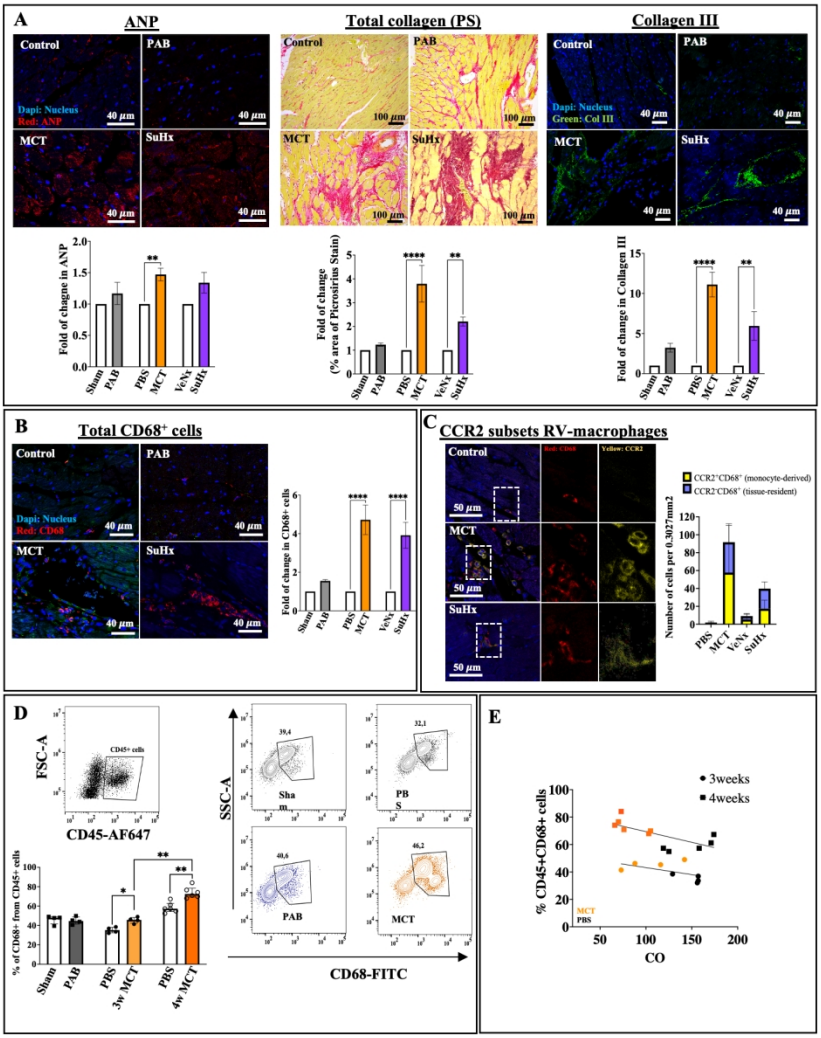

484x646mm (88 x 88 DPI)

AJRCCM Articles in Press. Published June 14, 2022 as 10.1164/rccm.202110-2274OC

Figure 2: Increased number of RV macrophages in PAH-rat models is marked by an increase in NLRP3 inflammasome activity

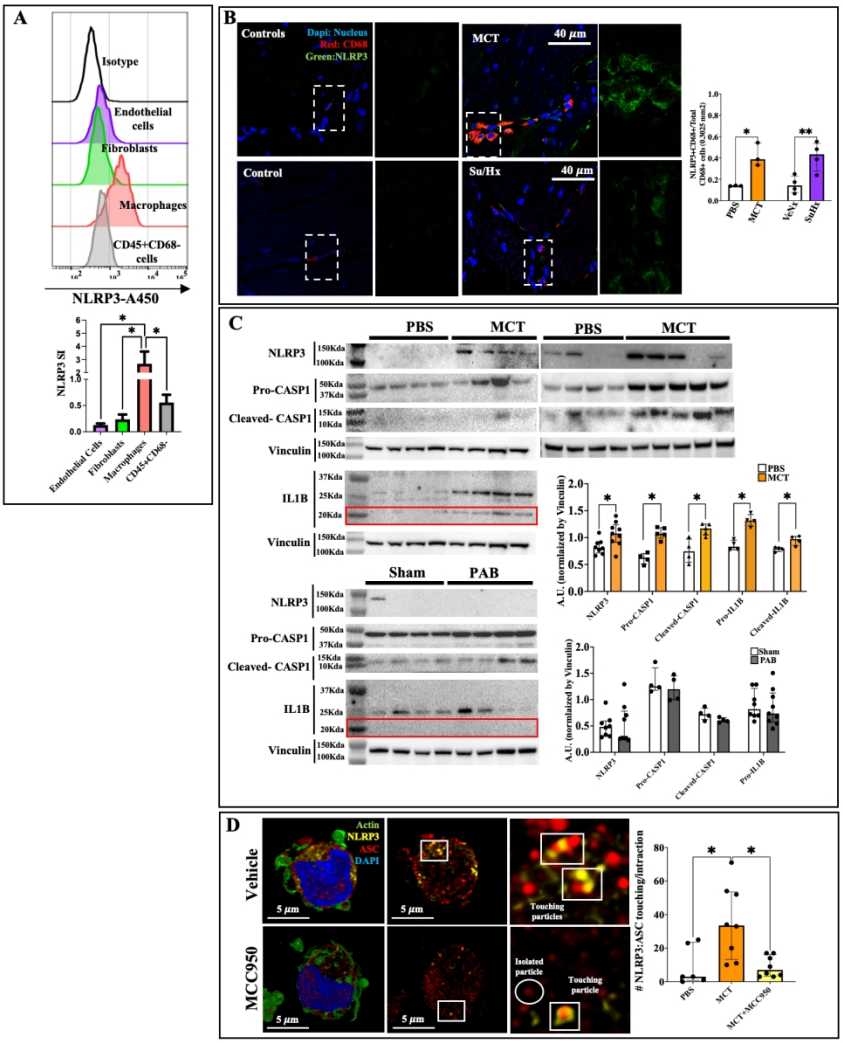

484x646mm (88 x 88 DPI)

AJRCCM Articles in Press. Published June 14, 2022 as 10.1164/rccm.202110-2274OC

Figure 3: SC-144 improves cardiac function, reduces RV macrophage number, and suppresses NLRP3 inflammasome and STAT3 activation

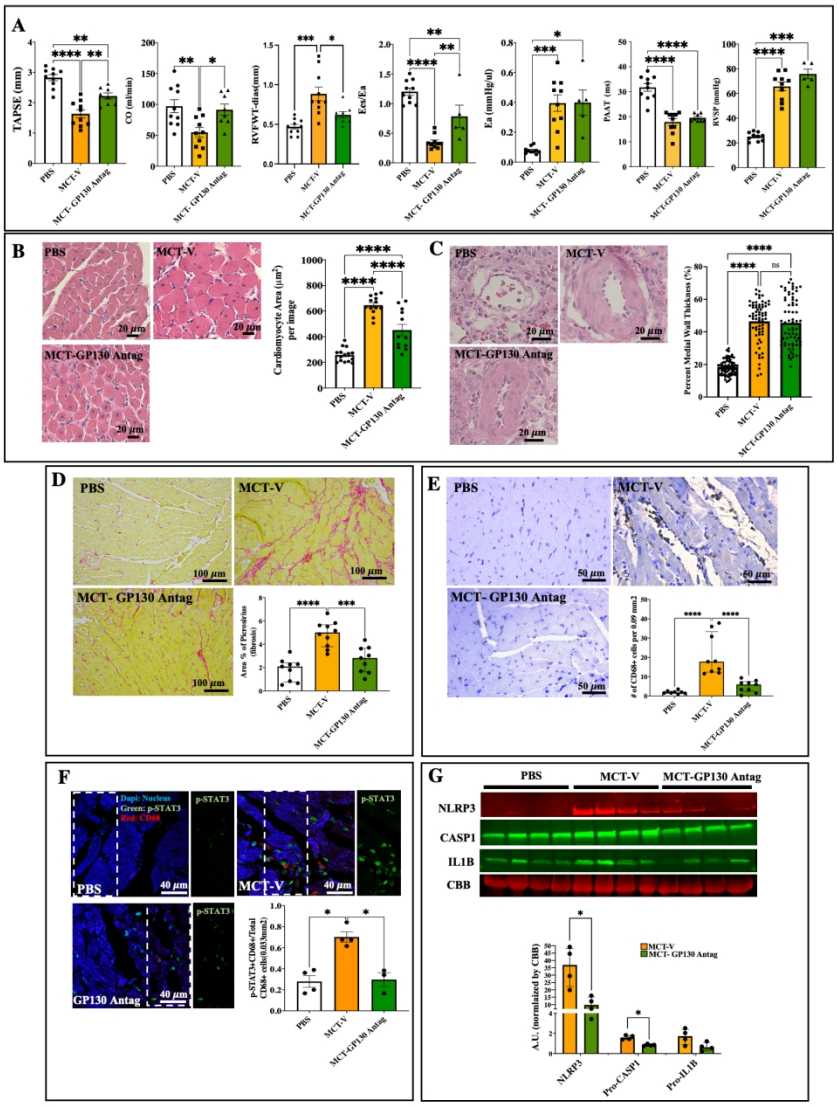

484x646mm (88 x 88 DPI)

AJRCCM Articles in Press. Published June 14, 2022 as 10.1164/rccm.202110-2274OC

Figure 4: MCC950 inhibits NLRP3 inflammasome activation and reduces mitochondrial damage in cardiomyocytes and RV fibrosis in PAH

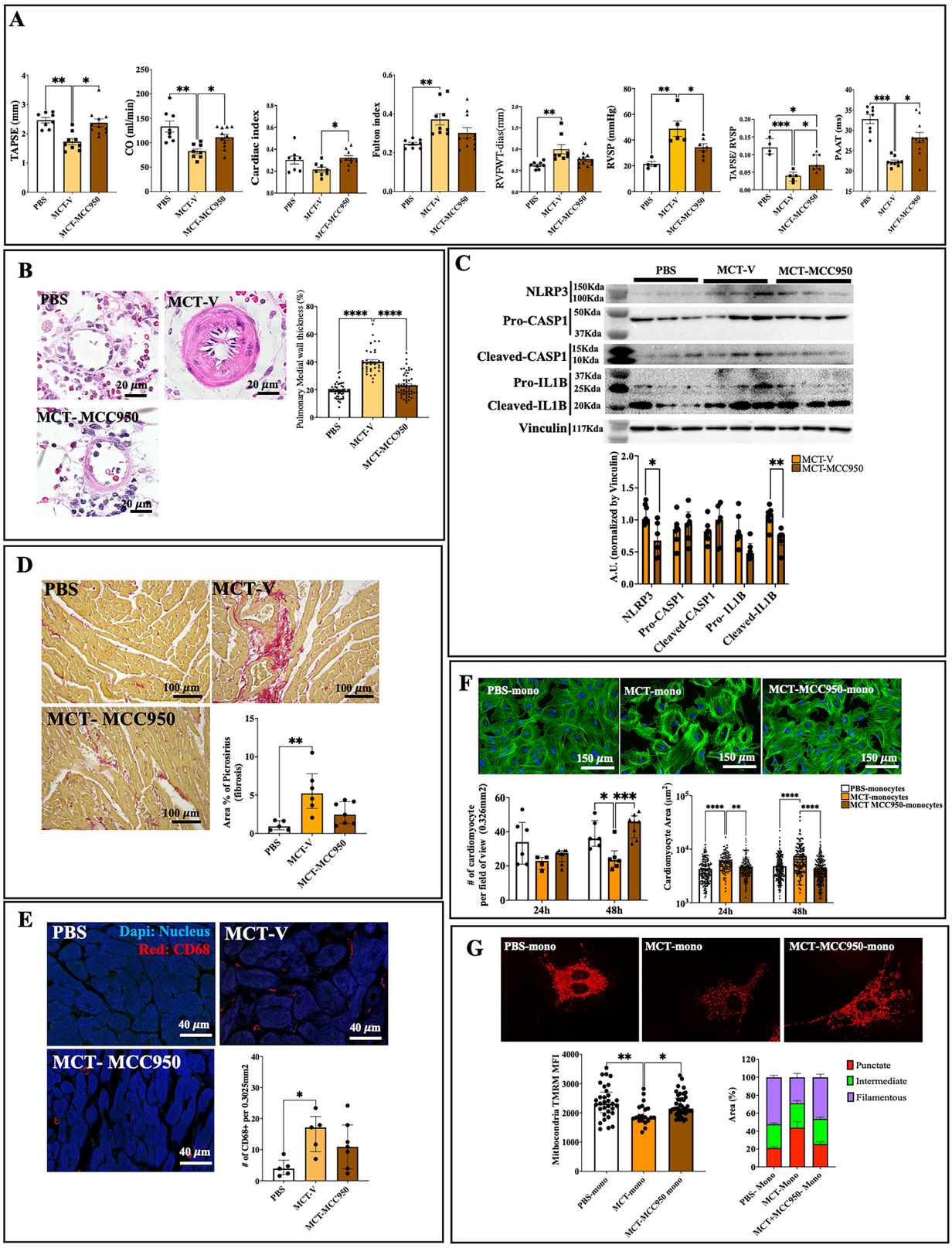

AJRCCM Articles in Press. Published June 14, 2022 as 10.1164/rccm.202110-2274OC

Figure 5: Increased incidence of macrophages and NLRP3 inflammasome activation in the RV from PAH patients with decompensated RVs

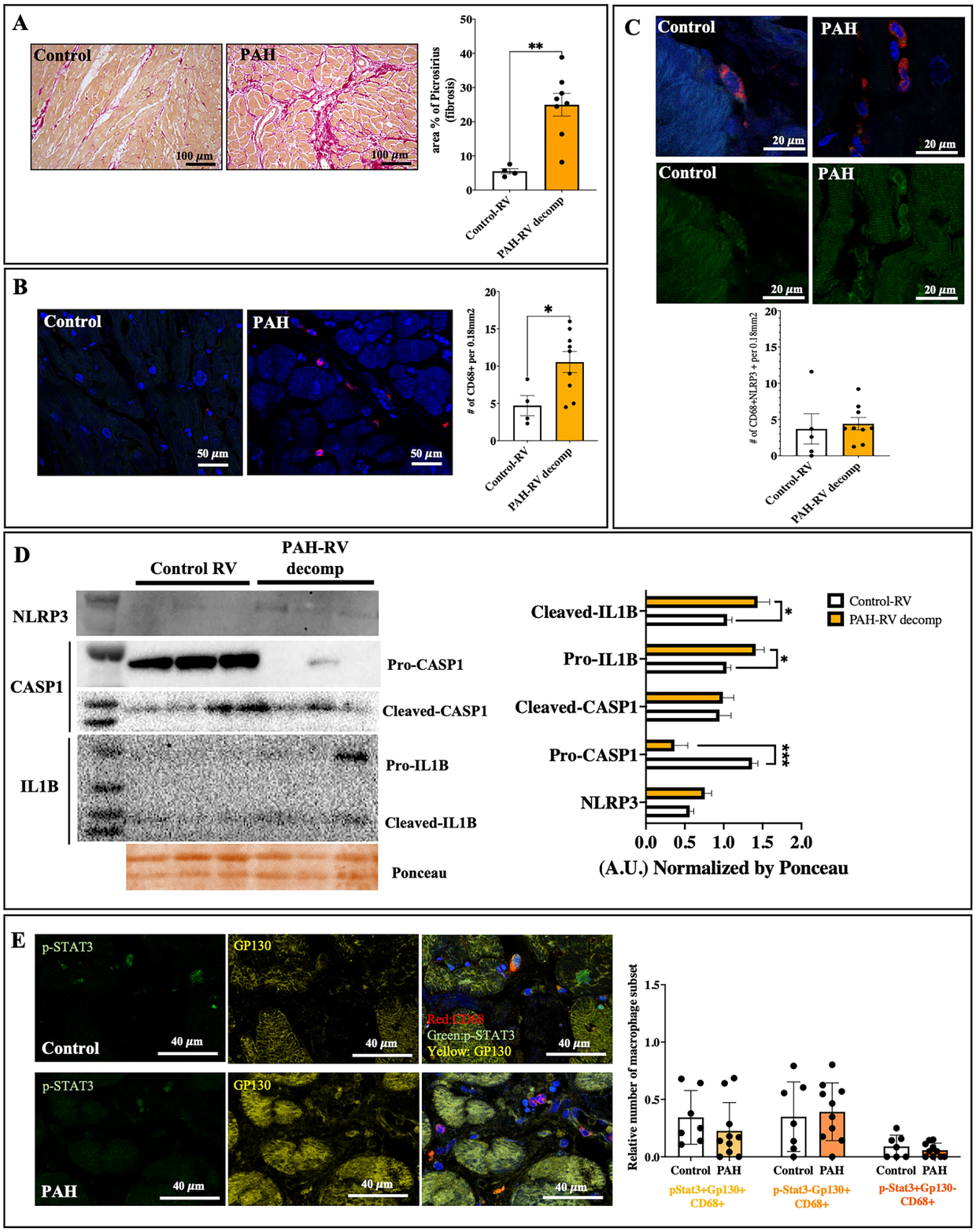

AJRCCM Articles in Press. Published June 14, 2022 as 10.1164/rccm.202110-2274OC

Figure 6: Distinctive M2 polarization of lung macrophages is consistent with regional heterogeneity in macrophage polarization between the RV and the lung in PAH

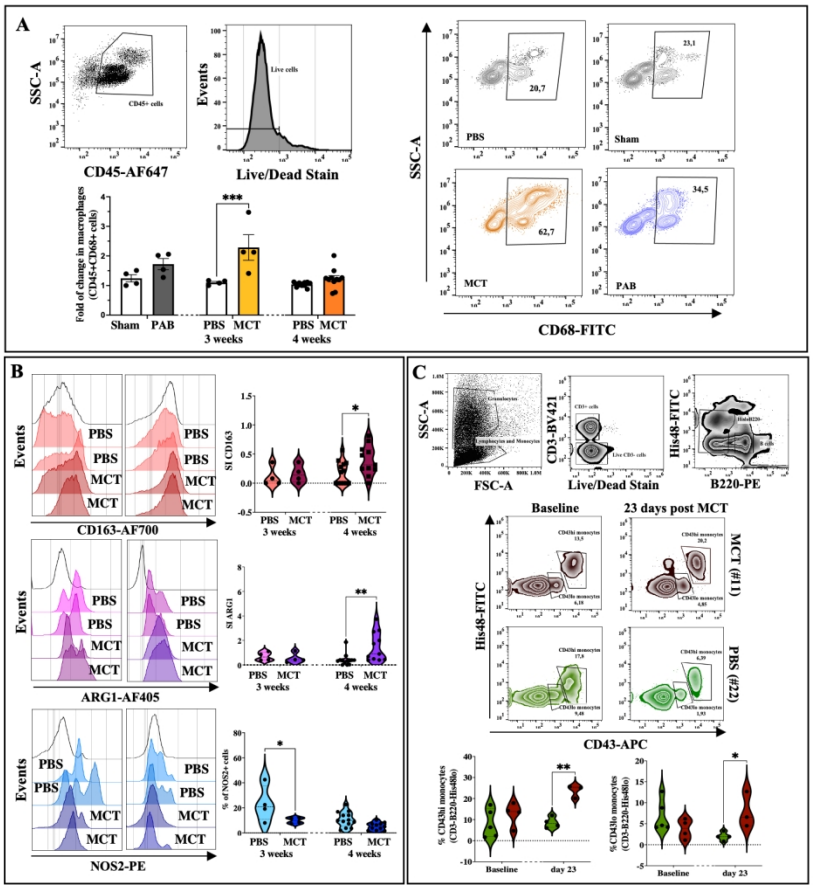

484x646mm (88 x 88 DPI)

AJRCCM Articles in Press. Published June 14, 2022 as 10.1164/rccm.202110-2274OC

Figure 7: PAH-RVF is triggered by Macrophage-NLRP3 activation and can be targeted by GP130 antagonism or NLRP3 inhibition

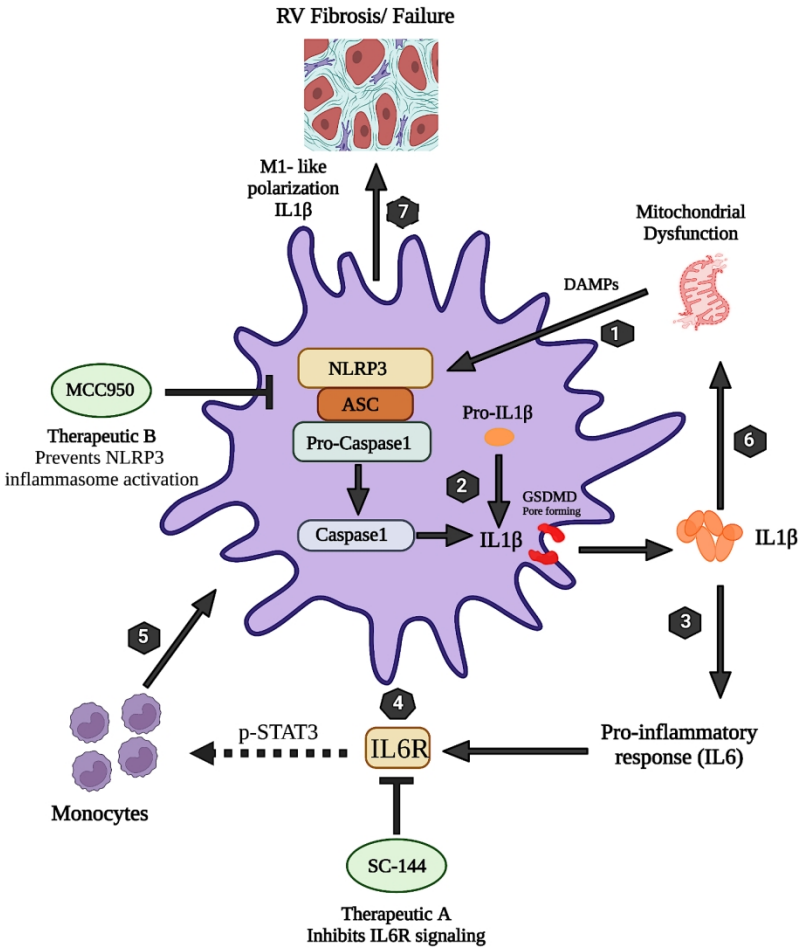

484x646mm (88 x 88 DPI)

AJRCCM Articles in Press. Published June 14, 2022 as 10.1164/rccm.202110-2274OC

Supplemental Material

Macrophage-NLRP3 Activation Promotes Right Ventricle Failure in Pulmonary Arterial Hypertension

Ruaa Al-Qazazi, Patricia D. A. Lima, Sasha Z. Prisco, Francois Potus, Asish Dasgupta, Kuang-Hueih Chen, Lian Tian, Rachel E. T, Bentley, Jeff Mewburn, Ashley Y. Martin , Danchen Wu, Oliver Jones, Donald H. Maurice, Sebastien Bonnet, Steeve Provencher, Kurt W. Prins, Stephen L. Archer

Supplemental Methods

1- Monocrotaline (MCT) rat model of PAH

Adult male Sprague-Dawley rats (8-9 weeks old, ~250 g; Charles River, QC, Canada) received a single subcutaneous injection of 60 mg/kg MCT (Sigma Aldrich, ON, Canada) in phosphate-buffered saline (PBS, Sigma Aldrich) as described before[1]. Food and water were supplied *ad libitum,* and weight was measured weekly. The development of PH was monitored for a 3 to 4-weeks period.

2- Sugen-5416 and hypoxia (SuHx) rat model of PAH

Adult Male Sprague-Dawley rats (8-9 weeks old, ~250 g Charles River, QC, Canada) received a single subcutaneous injection of Sugen-5416 (20mg/kg; biotechne Tocris, ON, Canada), followed by housing in the hypoxia chamber (Biospherix Ltd, USA) at 10% O2 for 3 weeks and normoxia (room air) for 3 weeks.

3- Pulmonary arterial banding (PAB) rat model of right ventricle hypertrophy (RVH)

AJRCCM Articles in Press. Published June 14, 2022 as 10.1164/rccm.202110-2274OC

Adult male Sprague-Dawley rats (6-7 weeks old, ~115 g) were anesthetized with a mixture of 100% O_2 and 5% isoflurane, intubated, and ventilated using a mechanical ventilator (Harvard Apparatus Canada, Saint-Laurent QC, Canada). Anesthesia was maintained via inhaled 3% isoflurane during the procedure, and an incision of the skin was made approximately 3 mm from the left sternal border level of the armpit. A left-sided thoracotomy was performed, creating an opening of 25 mm at the level of the second intercostal space. After opening the pericardium, the pulmonary trunk was separated from the aorta by blunt dissection. A size "small" (0.8 mm diameter) Weck® HorizonTM titanium clip (Teleflex, Markham, ON, Canada) was placed around the pulmonary artery using an applicator (Teleflex). This technique was modified from Andersen et al. surgery[2]. Following the pulmonary artery banding, the second and third ribs were approximated with 4-0 Vicryl (polyglactin) in an interrupted suture pattern. Before the last suture, a chest tube (1/32 in ID x 1/6 in OD Tygon tubing) was placed into the thorax, with the other end immersed in a bottle filled with sterilized saline. The outflow of the ventilator was shut off for 2-3 seconds to re-inflate the lungs, and residual air was aspirated from the chest. When no more air exited the chest tube, the last suture was tied, and the chest tube was removed. The muscle layers were opposed with 4-0 Vicryl (polyglactin) sutures, while the skin layer was closed using stainless steel wound clips. The animal was given time to recover on a heating pad (37^{o}C). The post-surgical assessment was conducted, and a subcutaneous injection of 0.05 mg/kg of Buprenorphine was given every 12 hours for 24-72 hours. The experimental length lasted 8 weeks; as the rats recovered and grew, the fixed stenosis remained, and the degree of obstruction increased.

4- Therapeutic intervention for the MCT rat model:

A) SC-144, a GP130 antagonist: Adult male Sprague-Dawley rats (n=30) received a single subcutaneous injection of MCT as previously described[5]. Rats were randomly divided into two groups. Starting at 14 days post-MCT, the first group received daily intraperitoneal injections

AJRCCM Articles in Press. Published June 14, 2022 as 10.1164/rccm.202110-2274OC

of SC-144 (10 mg/kg, APExBio Technology, Houston, TX) or vehicle for 10 days as previously described. SC-144 was dissolved in dimethyl sulfoxide (DMSO) to a 200 mg/mL concentration, diluted to 20 mg/mL in propylene glycol, and further added to 0.9% NaCl and 40% propylene glycol to achieve a final concentration of 10 mg/kg as previously described[4].

B) MCC950, an NLRP3 inflammasome inhibitor: Adult male (n=28) male Sprague-Dawley rats received a single subcutaneous injection of MCT as previously described[3]. Starting on day 14 post-MCT, rats received daily intravenous injections of MCC950 (6 mg/kg, InvivoGen, CP-456773; San Diego, CA) or vehicle for 10 days. MCC950 was dissolved in 40% dimethyl sulfoxide (DMSO; in 0.9% NaCl) to a concentration of 8.1 mg/ ml (stock solution). To achieve the working solution of 6 mg/kg, MCC950 stock solution was further diluted in 0.9% NaCl in a final volume of 1 ml per dose.

5- Cardiac ultrasound

Non-invasive doppler, 2-dimensional (2-D), and time-motion (M-mode) ultrasound was performed (before therapy and the day before euthanasia) using a high-frequency ultrasound (Vevo 2100, Visual Sonics, Toronto, ON, Canada) and a 37 MHz probe as previously described[1]. M-mode and 2-D mode were used to measure the following parameters: Using short access view, pulmonary artery acceleration time (PAAT), main pulmonary artery (PA) inner diameter and velocity time integral (VTI) were obtained at the level of the pulmonary outflow tract during mid-systole. The diastolic and systolic thickness of the RV free wall (RVFW) were obtained using the long access view. Tricuspid annular plane systolic excursion (TAPSE) was assessed using the apical 4 chamber view. Cardiac output (CO) was estimated (HR × VTI × ID^2/4), where HR is heart rate, VTI is systolic velocity time integral over the main PA flow obtained from pulsed-wave Doppler, and ID is the inner diameter of the main PA at mid-systole.

AJRCCM Articles in Press. Published June 14, 2022 as 10.1164/rccm.202110-2274OC

6- RV pressure-volume loop assessment by closed-chest catheterization

RV pressure-volume loop assessment was performed by invasive right heart catheterization (RHC), using closed-chest catheterization on anesthetized rats, as previously described[4]. Rats were initially anesthetized using a chamber containing gas anesthetic (oxygen 100%; isoflurane 3-4% for induction) and then positioned supine on a servo-controlled homeothermic pad. The temperature feedback probe was inserted in the rectum to monitor vital signs (desired body temperature was set at 37°C). The front and distal paws were taped down to the heated surface, and the rat's anesthesia was maintained via a nose cone, providing a mixture of 100% O_2 and 2% isoflurane. Ventilation settings were calculated using the ventilator's software, as previously described above. An inverted T-shaped mid-neck incision was made from the mandible to the sternum. Parotid glands were moved aside with forceps, and the thin muscle layer around the trachea was gently dissected to expose and isolate the right jugular vein. A surgical suture (4.0) was placed at the cephalic end of the vein, and gentle traction was applied using a needle holder. Two additional sutures were inserted beneath the jugular vein. A loose knot was placed to the middle suture and gently pulled toward the rat's head using a needle holder.

A micro incision was made near the proximal end of the vein, and a high-fidelity catheter was advanced into the jugular vein, proceeding distally using waveform guidance into the right atrium and then into the RV. RV pressure and magnitude (which reflects the blood and muscle value) were stabilized to generate an optimal PV loop (Y-axis pressure, X-axis magnitude). Following PV loop optimization, X-axis reporting was changed to report volume. Data were recorded continuously for 30-60 seconds using Scisense ADV500 Pressure-Volume Measurement System (Scisense pressure-volume catheter; Transonic, London, ON, Canada) and LabScribe2 software (iWorx, Dover, NH, USA). Subsequently, the catheter was gently withdrawn and soaked in a heparin/ sodium chloride solution. The distal suture was tightened to stop bleeding from the

AJRCCM Articles in Press. Published June 14, 2022 as 10.1164/rccm.202110-2274OC

jugular vein, and animals were humanely euthanized. Immediately after RHC, the cardiopulmonary unit was isolated and dissected. The RV and left ventricle plus septum (LV+S) were weighed. The heart and lungs were fixed in 4% paraformaldehyde (PFA) for histology or freshly collected for flow cytometry or protein analyses.

7- Immunohistochemistry

Paraffin sections (5 μm) were deparaffinized and hydrated. Antigen retrieval was achieved by microwave heating using a citrate buffer (10 mM, pH 6.0; 20 min) or by water bath (95^{o}C; 20 min) using Tris-EDTA buffer (10 mM pH 9). Following antigen retrieval, sections were allowed to cool and washed with PBS-tween 0.05% (PBS-T). For immunofluorescence staining, sections were blocked with 1 % or 3% Bovine Serum Albumin (BSA) for 30 min at room temperature, depending on the tissue and antibody. Sections were incubated overnight with primary antibodies at 4^{o}C (**Supplemental Table 1**). Next, sections were washed with PBS-T and incubated with conjugated secondary antibodies (**Supplemental Table 1**) for 1-hour at room temperature. Finally, slides were washed and mounted using ProLong Gold Antifade Mounting with DAPI (ThermoFisher; Waltham, MA, USA). The fluorescence-based imaging was performed using TCS SP8 laser scanning confocal microscope (SP8 Leica, Concord, ON, Canada) and the HC PL APO CS2 63x/1.40 oil objective. LAS-X software was used to acquire and analyse the images. In some of the IFs, the Field of View (FOV) tool (tile scanning) was used to obtain a large area of the field.

For immunoperoxidase, horseradish peroxidase (HRP) staining was conducted with mouse specific HRP/DAB (ABC kit ab64264, Abcam), as per the manufacturer's instruction. The imaging of HRP-based detection was performed using the Leica DM 4000 microscope (Leica), the 40x (air/0.65) objective, and the DFC310 FX camera. Images were analyzed using the LAS-X software (Leica) by a microscopist blinded to the treatment group.

AJRCCM Articles in Press. Published June 14, 2022 as 10.1164/rccm.202110-2274OC

As per quantification, only cells (macrophages or cardiomyocytes) with evident nucleoli were quantified in a field (0.3025mm^2). Collagen-III was measured as a percentage area of positivity in an image frame (Field of View image with 4 tiles using the 63x magnification objective/ 0.33mm^2 area). ANP mean fluorescence intensity (MFI) was quantified in individual cardiomyocytes by drawing regions of interest (ROIs) around these cells.

8- Hematoxylin and Eosin (H&E)

Paraffin sections of RV tissue and lung were deparaffinized and hydrated. Sections were stained using hematoxylin and eosin kit (H&E Staining Kit ab245880, Abcam). Images were acquired using Leica DM 4000 microscope (Leica) equipped with a DFC310 FX camera using a 20x objective and LASX software. Morphometric analysis was performed to measure cardiomyocytes size (hypertrophy) and pulmonary arterial wall thickness. In the heart, ROIs were drawn at the edge of cardiomyocytes to estimate their size. In the lung, the artery medial wall thickness was estimated by measuring the outer and inner layers of arteries in the transversal section, and it was calculated as follows:

% Artery medial wall thickness = 1- outer layer/inner layer x 100

9- ***In situ*** **collagen deposition quantification**

Paraffin sections of RV tissue were deparaffinized and hydrated. The nuclei were stained with Weigert's hematoxylin and subsequently stained with Picrosirius Red Stain as per the manufacturer's instruction (Sigma Aldrich; "Direct Red 80" Cat#365548). Images were acquired using Leica DM 4000 microscope (Leica) equipped with a DFC310 FX camera using a 20x objective and LASX software. The collagen fibers (defined by their red stain) were quantified using ImageJ by measuring the percentage of the red signal in the field.

10- Western Blotting

AJRCCM Articles in Press. Published June 14, 2022 as 10.1164/rccm.202110-2274OC

Total RV protein was prepared in anti-protease buffer (#9803; Cell Signaling Technologies, Beverly, MA, United States), and measured using the BCA protein reagent assay (A/B) (Thermo scientific; cat# 23228, 1859078). Seventy micrograms (70 µg) of protein were loaded on a 4-12% gradient polyacrylamide gel for electrophoretic separation using the SDS-PAGE method. Running buffer was prepared using 20X MOPS Buffer (novex: REF NP0001), 0.1% Bolt Antioxidant (Invitrogen: REF BT0005) and ddH_2O. Resolved proteins were transferred to polyvinylidene fluoride (PVDF) membranes (Initrogen: REF LC2002) and blocked in 5% milk. Immunoblotting was performed using the primary antibodies as described in **Supplemental Table 1**. Membranes were developed using ECL Western blot detection reagent (Amersham: REF RPN2232), imaged using ChemiDoc^{TM}MP imaging system (Bio-Rad Laboratories; Mississauga, ON, Canada) and analyzed with ImageJ.

11- Flow cytometry

RV and lung single-cell suspensions were obtained using organ-specific protocols. Upon animal euthanasia, the heart and lungs were harvested and kept in a calcium-free Hanks medium (Sigma Aldrich) until processing. The RV was minced and digested using the trypsin 0.25% and collagenase digestion buffer (in calcium-free Hanks) and the Eppendorf ThermoMixer C (37^{o}C,1500 RPM; 15 minutes; Eppendorf, Mississauga, ON, Canada). The supernatant was collected every 15 minutes (2 mL of RV single-cell suspension) 6 times. The left lung was dissected, minced, and digested using DNAase (100 mg/mL; Sigma Aldrich) and Liberase (13 WU/mL; Sigma Aldrich) for 30 minutes at 37^{o}C (2 cycles of 15 minutes). The cell suspensions of both RV and lung were filtered through a 70 µm cell strainer, and the total cell number was calculated (10^5 cells per tube). The LIVE/DEAD™ Fixable Near-IR Dead Cell Stain Kit (ThermoFisher Scientific L10119) was used to discriminate dead cells, as per the manufacturers' recommendation. Cells were stained using fluorescent-tagged antibodies against surface antigens

AJRCCM Articles in Press. Published June 14, 2022 as 10.1164/rccm.202110-2274OC

(**Supplemental Table 1**) and washed with FACS buffer. Cells were fixed with 2% PFA (15 minutes, 4°C), permeabilized using 0.2% saponin (15 minutes, 4°C), and stained with antibodies to detect intracellular antigens (**Supplemental Table 1**). The whole blood (50 μl) was stained using fluorescent-tagged antibodies (**Supplemental Table 1**) against surface antigens diluted in FACS buffer (5% BSA 0.1NaN3 in PBS) and heparin (Sigma Aldrich H4784; 50 ug/tube) for 30 minutes. Hemolysis was achieved using 1x RBC Lysis Buffer (eBioscience, Waltham, MA, USA). Cells were washed and resuspended in FACS buffer. The SH-800S cell sorter/cytometer (Sony Biotechnology San Diego, CA, USA) was used to acquire the cytometric data. The data was analyzed using the FlowJo™ (BD Life Sciences, USA).

12-*In vitro* activation of the NLRP3 inflammasome

Blood was collected in acid-citrate-dextrose (ACD) tubes via heart puncture, and the peripheral blood mononuclear cells (PBMC) were obtained using Histopaque-1077 (Sigma Aldrich), as per the manufacture's instruction. Primary culture of enriched blood monocytes was conducted in plastic-based dishes (Ibidi 15 µ-Slide 8-well chamber slides; Ibidi Inc., Fitchburg, USA; 80826). PBMCs were cultured in an FBS-rich medium for 4 hours to allow monocyte enrichment. The cells were washed with DMEM and cultured for additional 12 hours in the presence or absence of MCC950 (in an FBS-free medium; 37°C, 5% CO_2). Cells were then washed, and 1 µM of Nigericin (a potent NLRP3 inflammasome inducer; InvivoGen, San Diego, CA; CP-456773) was added to the culture (10, 20 and 30 minutes). The medium was removed, and cells were fixed with 2% PFA and stained with rabbit-anti NLRP3 (Alexa Fluor 568 goat-anti-rabbit IgG secondary antibody) and mouse-anti ASC (Alexa Fluor 647 goat-anti-mouse IgG secondary antibody) as detailed in **Supplemental Table 1**. Cells were counterstained with phalloidin (FITC, Abcam, ab235137) and DAPI. Imaging was performed using the TCS SP8 laser scanning confocal microscope (Leica). Images were deconvolved using the Huygens Essential Software (Scientific

AJRCCM Articles in Press. Published June 14, 2022 as 10.1164/rccm.202110-2274OC

Volume Imaging, Hilversum, Netherlands), and the 3D particle interaction (NLRP3:ASC) was quantified using the LASX software (Leica).

13- *In-vitro* assessment of rat cardiomyocytes co-cultured with monocytes (mitochondria, number, and hypertrophy)

Rat neonatal cardiomyocytes (Cat# R-CM-561; Lonza, Morristown, NJ, USA) were cultured in cardiac myocyte medium (Cat# 61-1(SC); Sciencell Research Laboratories, Carlsbad, CA, USA) supplemented with 10% Fetal Bovine Serum (Cat# 12484028; ThermoFisher Scientific, Waltham, MA, USA). Prior to plating the cells, culture dishes were coated with sterile gelatin from bovine skin (0.1% in water, Cat# G9391-100G; Sigma-Aldrich, Oakville, ON, Canada).

PBMCs from PBS, MCT-vehicle and MCT-MCC950 rats (n= 3, 3 and 4, respectively) were obtained as described above in section 12 using Histopaque-1077, and 1 x 10^6 PBMCs were plated in 35mm glass-bottom dishes (No 1.5 uncoated g-irradiated, P35G-1.5-14-C MatTek Corporation, Ashland, MA, USA) pre-coated with sterile gelatin. As blood monocytes represent 5- 10% of total PBMCs, we estimated 1 x 10^5 monocytes per dish. Enriched monocytes were treated or not with Nigericin for 10 minutes as described above in section 12 (***In vitro* activation of the NLRP3 inflammasome**). Monocyte culture was washed three times with cardiac myocyte medium, and cardiomyocytes were added to the culture at a density of 1 x 10^5 cells per dish. Co-culture was conducted for 24 or 48 hours. Cells were then incubated with 2mM Tetramethylrhodamine Methyl Ester Perchlorate (TMRM, Cat# T668; ThermoFisher Scientific) in 2mL supplemented cardiac myocyte medium for 30 minutes at 37°C in the dark. Dye was removed, and dishes were washed with cardiac myocyte medium. Live imaging was then performed using a stage top incubator (OkoLab; Ambridge, USA) with a temperature, gas and humidity controller connected to the TCS SP8 laser scanning confocal microscope. TMRM mean fluorescence intensity (MFI) was measured as a surrogate for mitochondrial membrane potential,

AJRCCM Articles in Press. Published June 14, 2022 as 10.1164/rccm.202110-2274OC

and mitochondrial fragmentation was assessed through machine learning[5]. Cells were then fixed with 4% PFA, and stained with phalloidin and DAPI. Cardiomyocyte's number and area (ROIs) were assessed at both 24- and 48-hours' time points.

Supplemental table 1: Antibody information

Antibody	*Technique*	*Working dilution*	*Cat#/Manufacturer*
Primary antibodies used with rat's samples			
Rabbit Anti-NLRP3	- Immunofluorescence - Western blot - Flow Cytometry	- 1:400 - 1:1000 - 1:50	NBP2-12446-Novus biological
Mouse anti- Rat CD68	- Immunofluorescence	- 1:200	ab31630- Abcam
Rabbit anti-IL1B	- Western blot	- 1:1000	ab9722- Abcam
Rabbit anti-Caspase1	- Western blot	- 1:1000	ab179515- Abcam
PE Mouse anti-rat CD31	- Flow Cytometry	- 1:100	555027-BD Bioscience
Alexa Fluor 700 Mouse anti-rat CD90	- Flow Cytometry	- 1:100	202528-Biolegend
Alexa Fluor 647 Mouse anti-rat CD45	- Flow Cytometry	- 1:50	202211- Biolegend
Alexa Fluor 700 Mouse anti-rat CD163	- Flow Cytometry	- 1:100	NBP2-39099AF700-Novus Biologicals
Alexa Fluor 488 Mouse anti-rat CD68	- Flow Cytometry	- 1:100	NB600-985AF488Novus Biologicals
Rabbit anti-ARG1	- Flow Cytometry	- 1:50	NBP1 3273155- Novus Biologicals
PE Mouse anti-NOS2	- Flow Cytometry	- 1:25	sc-7271 PE - Santa Cruz
Rabbit anti-P-STAT3	- Immunofluorescence	- 1:50	MA5-32089- Invitrogen
Goat anti- rat ANP	- Immunofluorescence	- 1:100	NBP1-97752- Novus Biologicals
Mouse anti- rat collagen-III	- Immunofluorescence	- 1:100	Ab-6310- Abcam
Rabbit anti rat CCR2	- Immunofluorescence - Immunofluorescence	- 1:100 - 1:100	Ab-273050 ER1901-37

AJRCCM Articles in Press. Published June 14, 2022 as 10.1164/rccm.202110-2274OC

Rabbit anti mouse GSDMD					
Primary antibodies used with human's samples					
Mouse anti-human CD68	-	Immunofluorescence	-	1:100	14-0688-82- eBioscience
Rabbit anti-NLRP3	-	Immunofluorescence	-	1:400	NBP2-12446- Novus biological
	-	Western blot	-	1:100	
Rabbit anti-IL1B	-	Western blot	-	1:1000	ab9722- Abcam
Rabbit anti-Caspase1	-	Western blot	-	1:1000	ab179515- Abcam
Rabbit anti-P-STAT3	-	Immunofluorescence	-	1:50	MA5-32089- Invitrogen
Rat anti-Human GP130	-	Immunofluorescence	-	1:100	MA5-23922- Invitrogen
Secondary antibodies					
Alexa Fluor 488 goat-anti-rabbit IgG	-	Immunofluorescence	-	1:500	011038- Life Technologies
Alexa Fluor 568 goat anti-mouse IgG	-	Immunofluorescence	-	1:500	A11031- Life Technologies
Alexa Fluor 405 goat -anti-rabbit IgG	-	Flow Cytometry	-	1:200	A-31556-Thermo-Fisher
Alexa Fluor 647 goat-anti-mouse IgG	-	Immunofluorescence	-	1:400	A-21236 - Invitrogen
HRP goat-anti-rabbit	-	Western blot	-	1:1000	NA934-GE- Healthcare Life Sciences
Cy3 goat anti-rat	-	Immunofluorescence	-	1:400	112-165-003- Jackson Immuno Research Laboratories
Alexa Fluor 647 goat-anti-rabbit IgG	-	Immunofluorescence	-	1:400	A-32733 - Invitrogen
Isotype Controls					
PE Mouse IgG1,k isotype	-	Flow Cytometry	-	1:50	40011- Biolegend
Alexa Fluor 700 Mouse IgG1, k isotype	-	Flow Cytometry	-	1:50	400143- Biolegend
Alexa Fluor 488 Mouse IgG1 isotype	-	Flow Cytometry	-	1:50	400132- Biolegend
Rabbit Polyclonal Antibody	-	Flow Cytometry	-	1:50	910801- Biolegend

AJRCCM Articles in Press. Published June 14, 2022 as 10.1164/rccm.202110-2274OC

Supplemental table 2: MCT Rats cardiac function information

	MCT-model				
	PBS	**MCT- 3 weeks**	***p*-value**	**MCT- 4 weeks**	***p*-value**
Cardiac Ultrasound					
†RVFWT– dias (mm)	**0.64±0.024**	**-**	**-**	**1.36±0.166**	**0.0006*** **
TAPSE	**2.88 ± 0.094**	**2.434±0.161**	**0.053**	**1.76±0.130**	**0.0012** **
‡CO (mL/min)	**122.40±5.195**	**105.7±13.08**	**0.013***	**56.57±5.879**	**0.0006*** **
§PAAT (ms)	**31.71±1.409**	**24.67±1.629**	**0.011***	**20.01±1.492**	**0.0012** **
RHC					
††RVSP (mmHg)	**22.69±1.022**	**38.24±1.022**	**0.009** **	**51.32 ±2.510**	**0.0007*** **
RVEDP	**0.946±0.304**	**4.563±0.496**	**0.009***	**4.851±0.568**	**0.0007*** **
EF	**78.66±1.721**	**73.64±1.721**	**0.257**	**51.19±4.914**	**0.0007*** **
CO (mL/min)	**139.1 ± 4.120**	**148.6±18.99**	**0.761**	**54.38±9.33**	**0.0006*** **
§§CI	**0.334±0.088**	**0.29±0.042**	**0.449**	**0.207±0.025**	**0.025***
Anatomical parameter					
Fulton Index	**0.213 ± 0.014**	**-**	**-**	**0.311 ± 0.041**	**0.004** **

Values are presented as Mean± SEM.

Non-parametric T test (Mann- Whitney) was used to compare MCT, SuHx and PAB rats with their respective controls: *(p≤0.05), **(p≤0.01), *(p≤0.001).**

†RVFWT– dias= Right ventricular free wall thickness in diastole, ‡CO= cardiac output, § PAAT= pulmonary artery acceleration time, ††RVS*P* =*R*ight ventricular systolic pressure, §§CI= cardiac index

PBS N=6, MCT-4 weeks N=8, MCT-3 weeks N=4

AJRCCM Articles in Press. Published June 14, 2022 as 10.1164/rccm.202110-2274OC

Supplemental table 3: PAH-Patient Information

	Diagnostic	***Comorbidities***
Male ID samples		
A117	Ebstein disease	Ebstein disease, Type I diabetes.
A132	Tetralogy of Fallot (ToF)	ToF surgery, atrial flutter, back and knees osteoarthritis.
A14	SSc-PAH	Chronic cholestasis, Dyslipidemia, Diabetes, Hypertension.
A137	iPAH	Dyslipidemia, hypothyroidism, aortic stenosis, chronic renal failure. Pacemaker. Cirrhosis cardiomyopathy. Paroxysmal atrial fibrillation. Thrombocytopenia.
A200	limited SSc-PAH	Dyslipidemia, Hypertension, atrial flutter.
Female ID samples		
A31	Post-cure TOF decompensated no PAH, RV failure	Diabetes
A08	**SSc-PAH**	Hypertension, hyponatremia, asthma, iron deficiency anemia.
A27	Limited SSc-PAH	Severe scleroderma PAH with digestive symptoms. Raynaud syndrome associated with digital ulcers.
A71	PAH + Eisenmenger syndrome	Hypertension. Eisenmenger syndrome.
A83	Portal-PAH (PPHTN)	PAH secondary to hepatic cirrhosis (Child class B). Previous smoking.
A101	Limited SSc-PAH + Crest syndrome	Pulmonary capillary hemangiomatous. Primary biliary cirrhosis. Dyslipidemia. Chronic renal failure.
A113	iPAH (PVOD-Veno-occlusive disease unlikely)	Hypertension. Chronic renal failure. Rectal cancer. Hypertension. Pulmonary fibrosis. Limited scleroderma. Raynaud disease, Sjogren disease.
A119	Heritable-PAH (BMPR2)	**N/A**
A160	iPAH (PVOD-veno-occlusive disease unlikely)	Dyslipidemia, Type 2 Diabetes, Hypertension, Nocturnal hypoxemia. Ascites.

AJRCCM Articles in Press. Published June 14, 2022 as 10.1164/rccm.202110-2274OC

Supplemental references:

1. Tian L, Potus F, Wu D, et al. Increased Drp1-mediated mitochondrial fission promotes proliferation and collagen production by right ventricular fibroblasts in experimental pulmonary arterial hypertension. *Front Physiol*. 2018;9(JUL). doi:10.3389/fphys.2018.00828
2. Andersen S, Schultz JG, Holmboe S, et al. A pulmonary trunk banding model of pressure overload induced right ventricular hypertrophy and failure. *J Vis Exp*. 2018;2018(141):e58050. doi:10.3791/58050
3. van Hout GPJ, Bosch L, Ellenbroek GHJM, et al. The selective NLRP3-inflammasome inhibitor MCC950 reduces infarct size and preserves cardiac function in a pig model of myocardial infarction. *Eur Heart J*. 2017;38(11):828-836. doi:10.1093/eurheartj/ehw247
4. Potus F, Martin AY, Snetsinger B, Archer SL. Biventricular Assessment of Cardiac Function and Pressure-Volume Loops by Closed-Chest Catheterization in Mice. *J Vis Exp*. 2020;(160). doi:10.3791/61088
5. Wu D, Dasgupta A, Chen KH, et al. Identification of novel dynamin-related protein 1 (Drp1) GTPase inhibitors: Therapeutic potential of Drpitor1 and Drpitor1a in cancer and cardiac ischemia-reperfusion injury. *FASEB J*. 2020;34(1):1447-1464. doi:10.1096/FJ.201901467R

5. Xu S, Grande F, Garofalo A, Neamati N. Discovery of a novel orally active small molecule gp130 inhibitor for the treatment of ovarian cancer. *Mol Cancer Ther*. 2013; 12:937-949 doi**:** 10.1158/1535-7163.MCT-12-1082

AJRCCM Articles in Press. Published June 14, 2022 as 10.1164/rccm.202110-2274OC

Supplemental Figures and Figure Legends

Figure 1

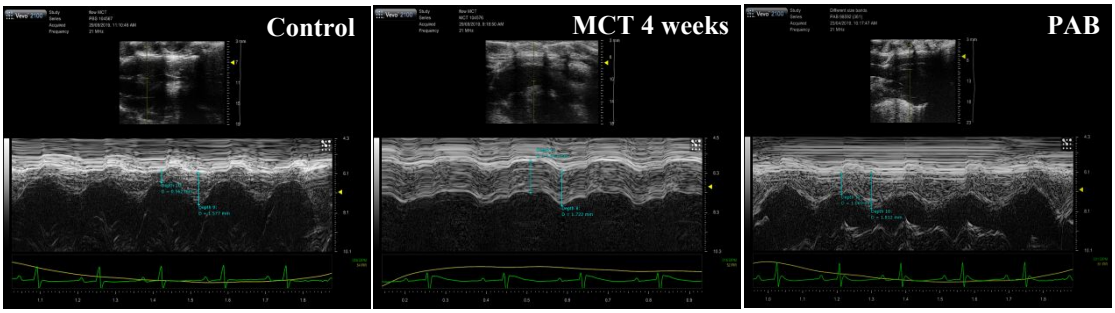

Figure 1(A): Cardiac ultrasound assessment of RV function. The Image demonstrates the RV free wall thickness (RVFWT) in diastole and systole measurement in Control, 4-weeks MCT and PAB rats and confirms the RV hypertrophy in both MCT and PAB rats.

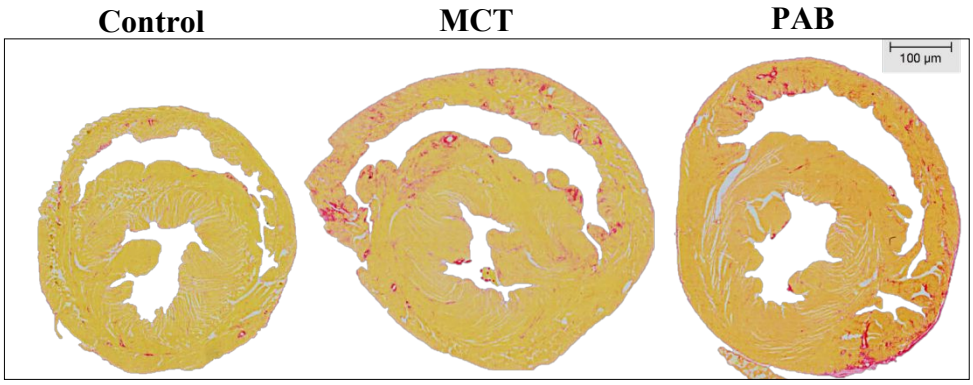

Figure 1 (B): RV hypertrophy was observed in MCT and PAB rats (bar=100 um) compared to their respectively controls (n= 5/group; *p= 0.0004* and *p= 0.024*).

AJRCCM Articles in Press. Published June 14, 2022 as 10.1164/rccm.202110-2274OC

Figure 2

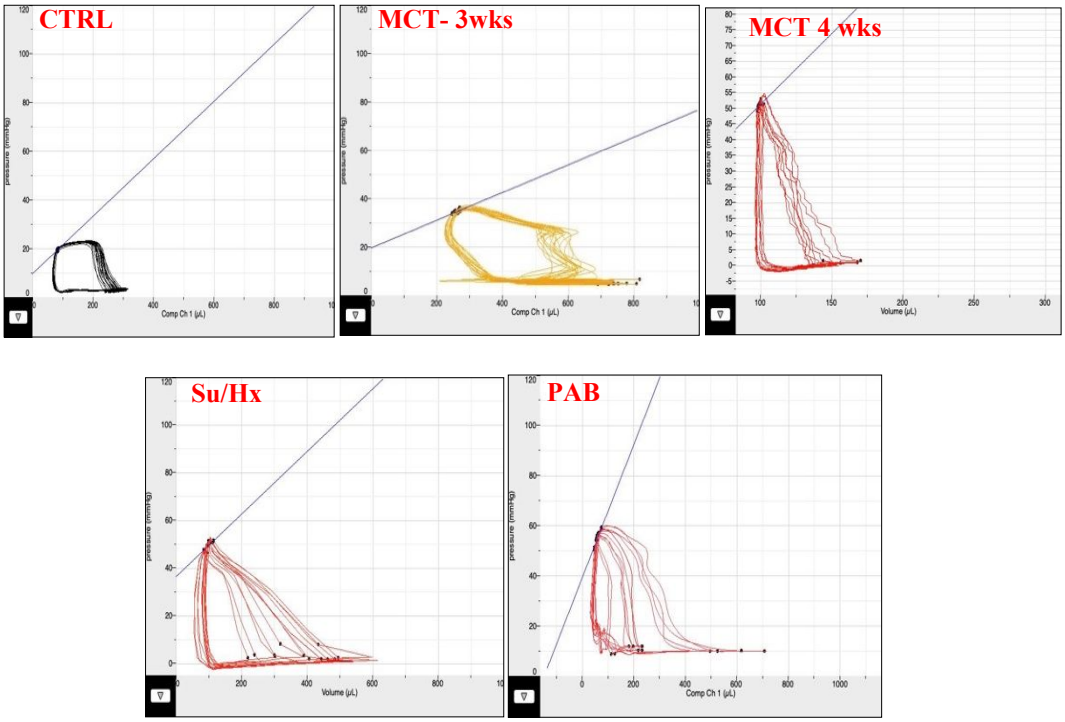

Figure 2 (A): Representative figure of the pressure volume (p-v) loop data of control, 3-weeks MCT, 4-weeks MCT, SuHx and PAB models.

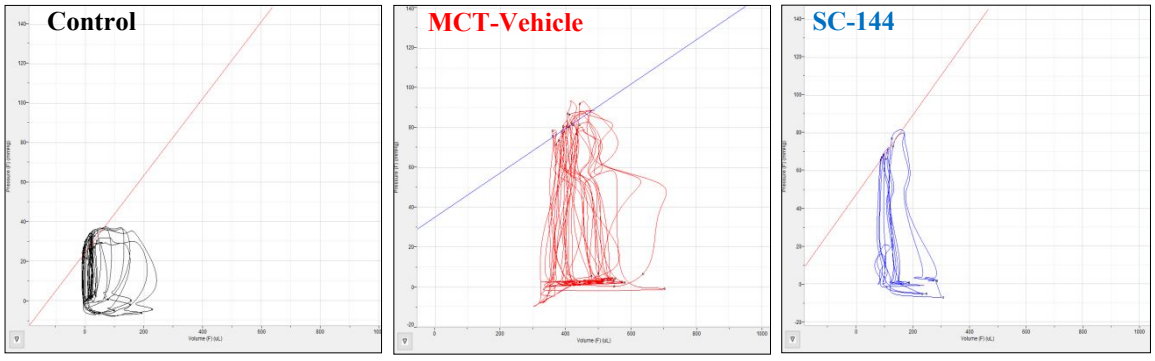

Figure 2 (B): RepresentitiveRepresentative figures of the pressure- volume (p-v) loop data of control, MCT-vehicle and MCT-GP130 antagonist treatment.

AJRCCM Articles in Press. Published June 14, 2022 as 10.1164/rccm.202110-2274OC

Figure 3

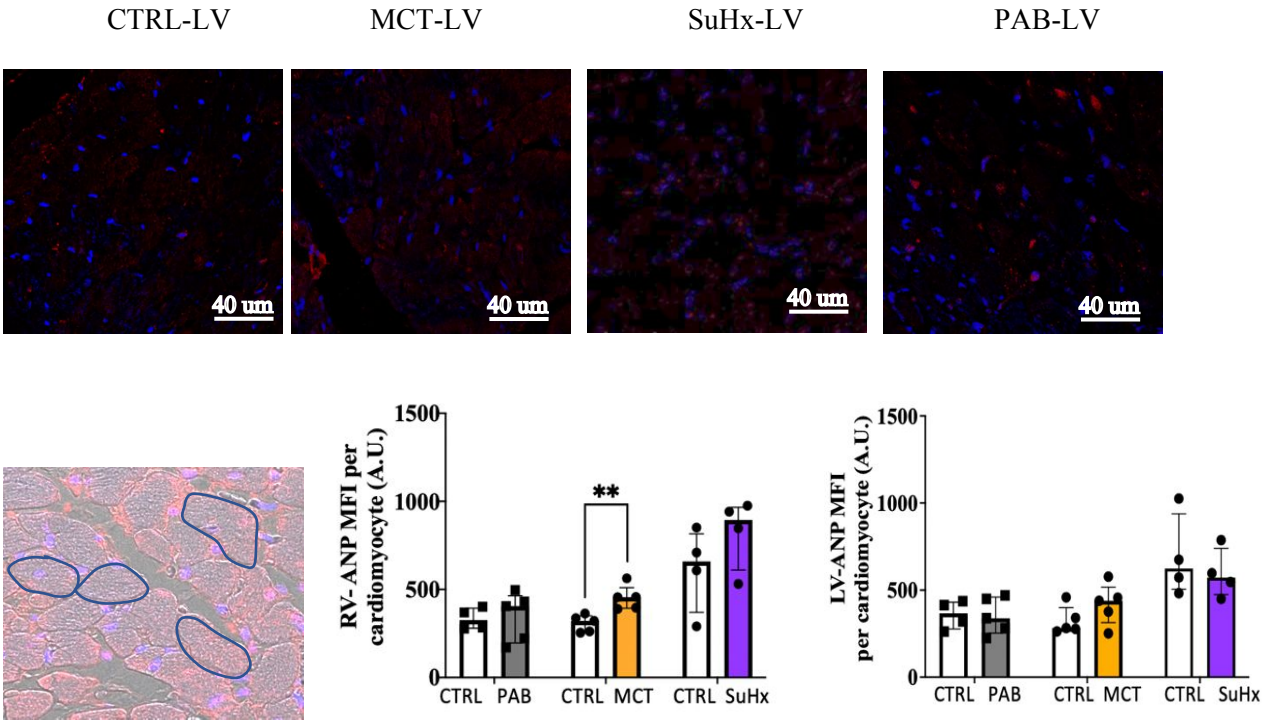

Figure 3 (A): Mean fluorescence intensity (MFI) quantification of ANP signal in the LV of MCT, PBS, PAB, Sham, SuHx and their control rats (red signal, n=4-5 rats/group). The LV tissue was stained with goat anti-rat ANP followed by anti-goat conjugated with Alexa Fluor 647. Images were taken using confocal microscope. The MFI of ANP expression in individual cardiomyocytes was measured using regions of interest (ROI) as demonstrated. A minimum of 5 images was taken per rat (5- 10 cardiomyocytes per image; 25-50 cardiomyocytes per rat). No significant difference was found when groups were compared.

AJRCCM Articles in Press. Published June 14, 2022 as 10.1164/rccm.202110-2274OC

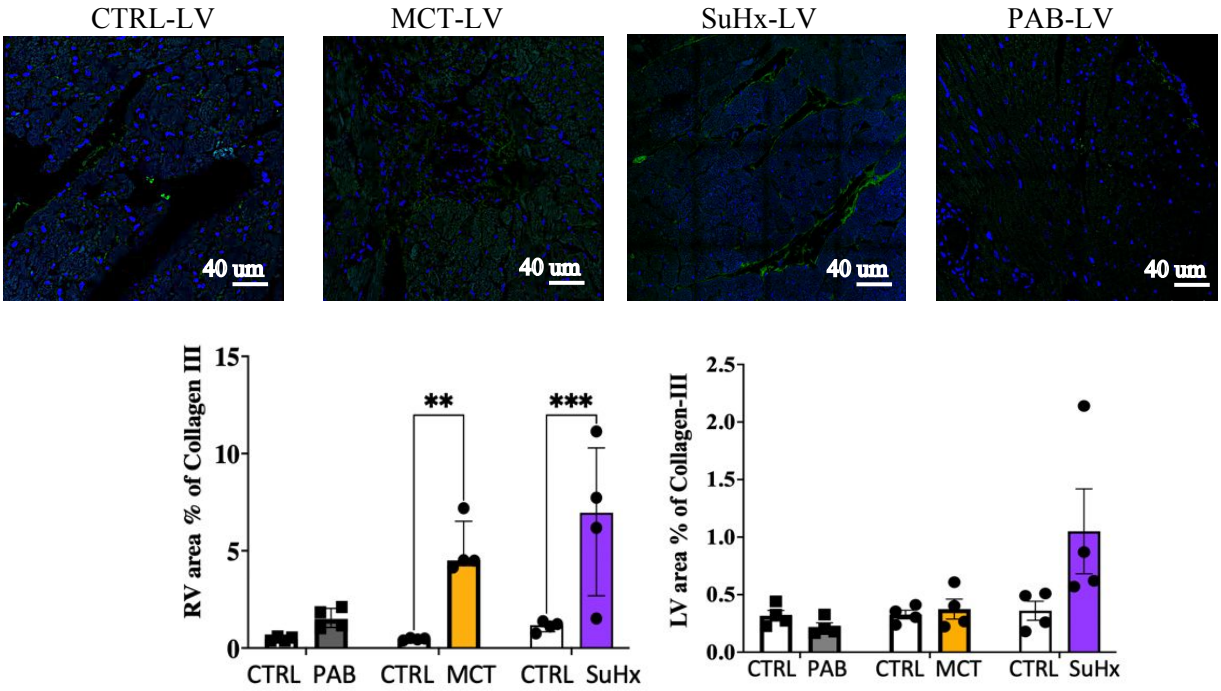

Figure 3 (B): The collagen III in the LV tissue of MCT, PBS, PAB, Sham, SuHx and their control rats (green signal, n=4-5 rats/group) was quantified as the percentage area of positivity in an image frame (Field of View images with 4 tiles using the 63x magnification objective/ 0.33mm^2 area). The tissue was stained with the rabbit-anti- rat collagen-III, followed by anti-rabbit conjugated with Alexa Fluor 488 (green). No significant difference was found when LV in different groups were compared.

AJRCCM Articles in Press. Published June 14, 2022 as 10.1164/rccm.202110-2274OC

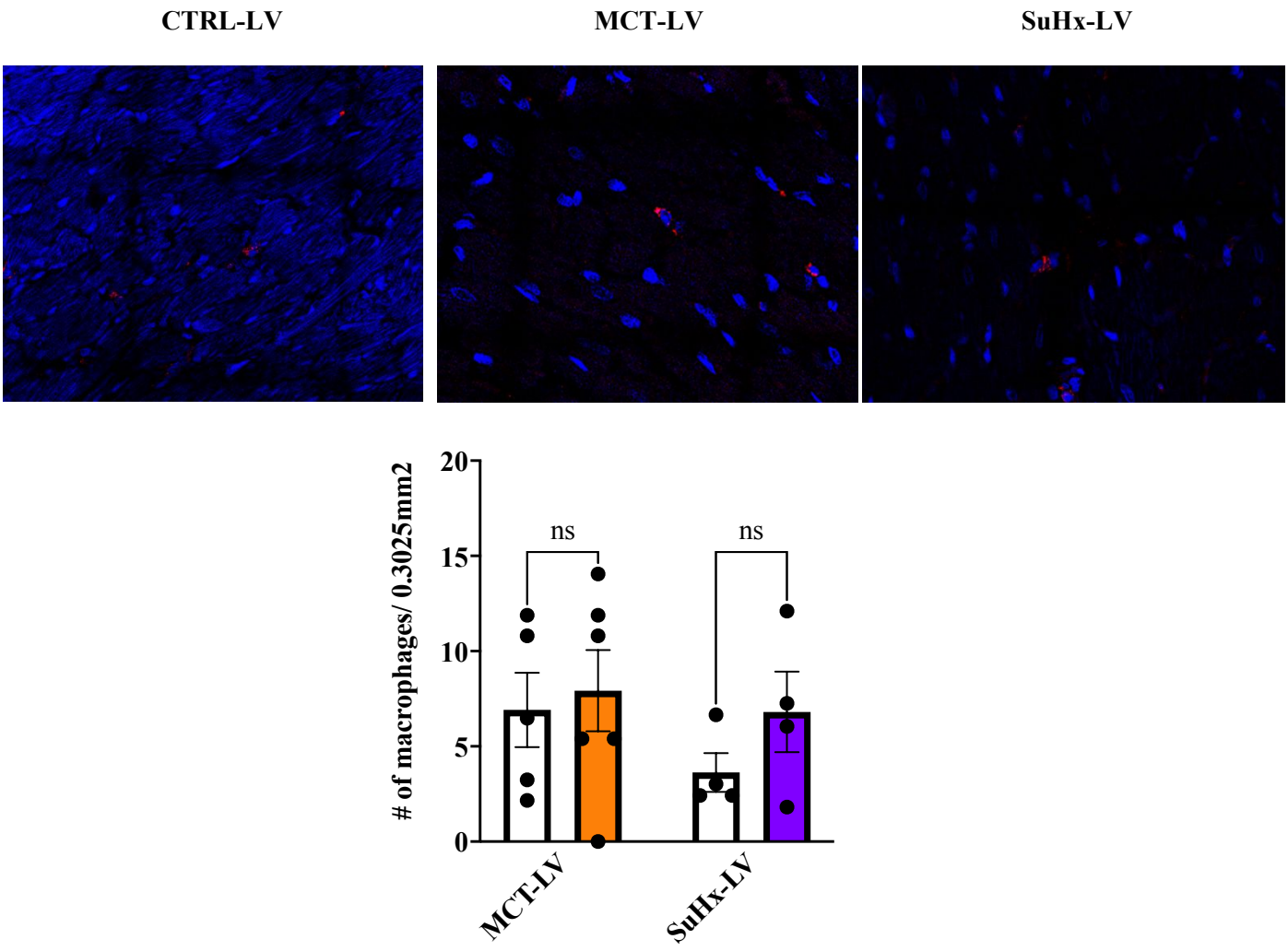

Figure 3 (C): Macrophages quantification in the LV tissue of MCT and SuHx rats and their control rats (red signal, n=4-5rats/group). No difference were found between MCT *vs* PBS or SuHx *vs* VeNx. As the RV, LV tissue was stained with mouse anti-rat CD68 followed by anti-mouse conjugated with Alexa Fluor 555. Images were taken using confocal microscope.

AJRCCM Articles in Press. Published June 14, 2022 as 10.1164/rccm.202110-2274OC

Figure 4

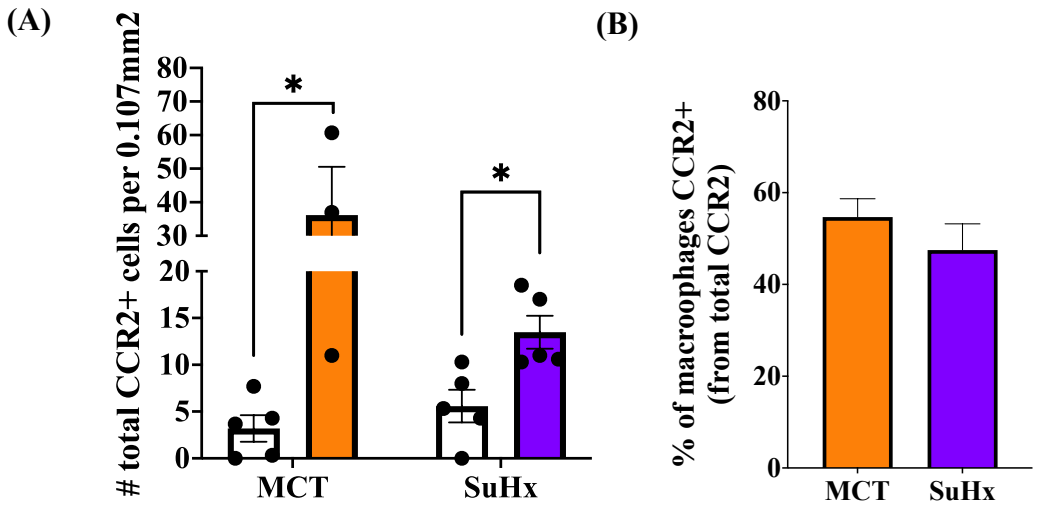

Figure 4 (A): The quantificaiton of total CCR2 cells in the RV of MCT and SuHx rats showed that CCR2^{+} cells were significantly elevated in both PAH-rat models compared to controls (MCT: *p=0.357* and SuHx: *p=0.0159*; non-parametric Mann Whitney test; n=3-5 **rats**/group). (B) Macrophages represent 54.67% and 47.49% of total cells expressing CCR2 after MCT and SuHx induction of PAH.

AJRCCM Articles in Press. Published June 14, 2022 as 10.1164/rccm.202110-2274OC

Figure 5

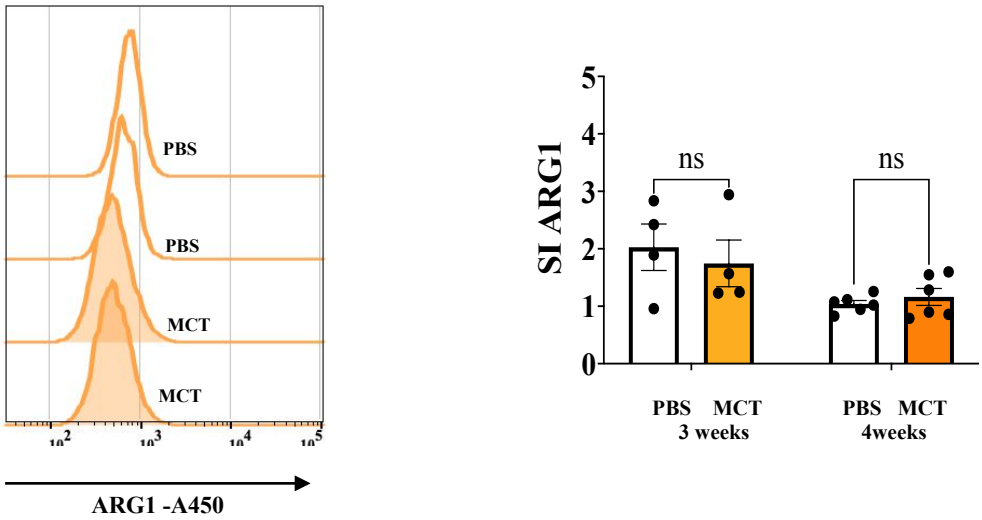

Figure 5: The polarization of RV macrophages was determined by measuring the expression level of ARG1 (an M2-like macrophage marker). When comparing MCT-RV-macrophages to their controls, no difference in ARG1 expression was detected (n=4 rats/group; 3 weeks *p=0.949* and 4 weeks *p>0.999*).

AJRCCM Articles in Press. Published June 14, 2022 as 10.1164/rccm.202110-2274OC

Figure 6

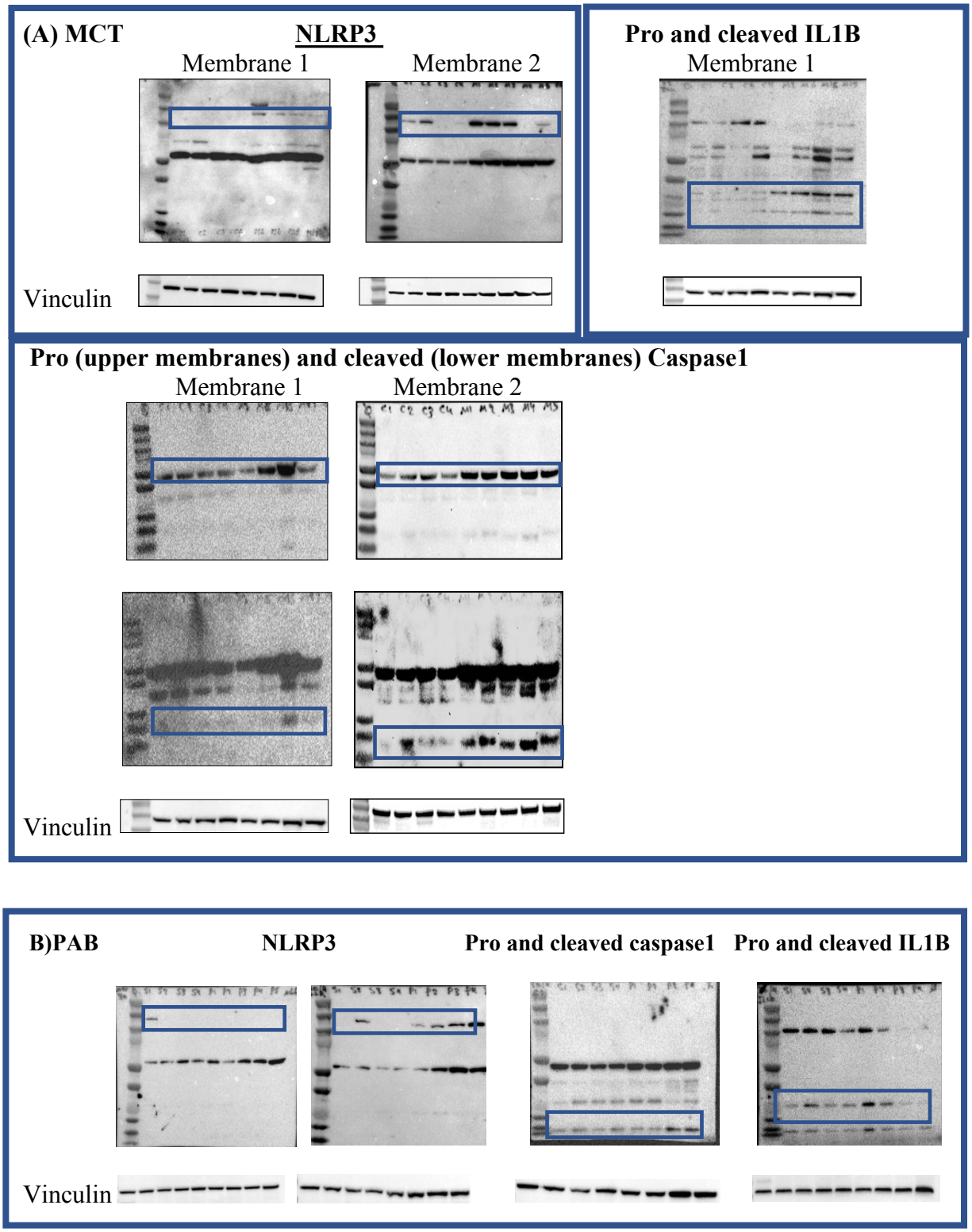

Figure 6: Complete set of Western blot membranes used to quantify NLRP3, Caspase 1 and IL1B in MCT and PAB RVs with controls (n= 8 MCT, 9 PBS, 4-8 PAB and 4-8 shams).

AJRCCM Articles in Press. Published June 14, 2022 as 10.1164/rccm.202110-2274OC

Figure 7

(A)

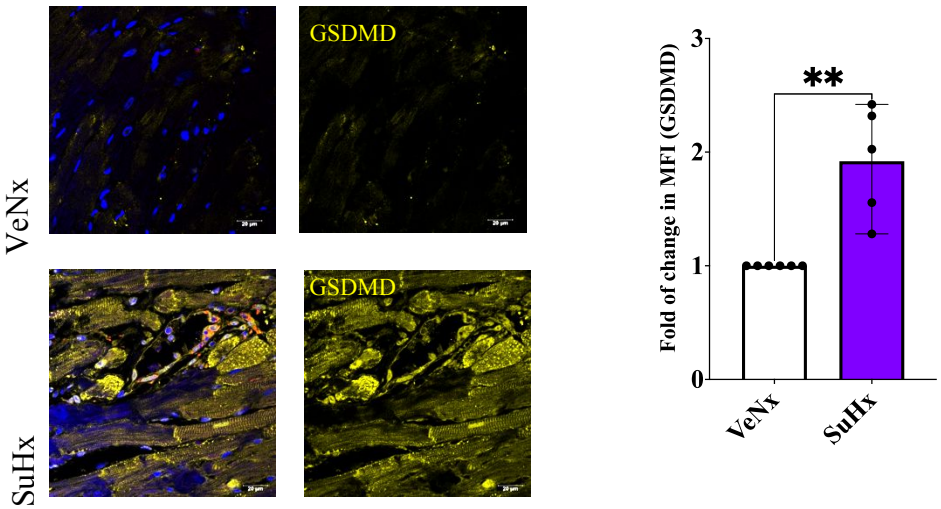

Figure 7A: The mean fluorescence intensity (MFI) of the pore forming protein Gasdermin D (GSDMD) (Alexa-fluor 647) was measured via confocal microscopy and a fold of change analysis shows a significant increase in SuHx-RV compared to control (n=5 rats/group; *p=0.002;* Mann Whitney test*)*.

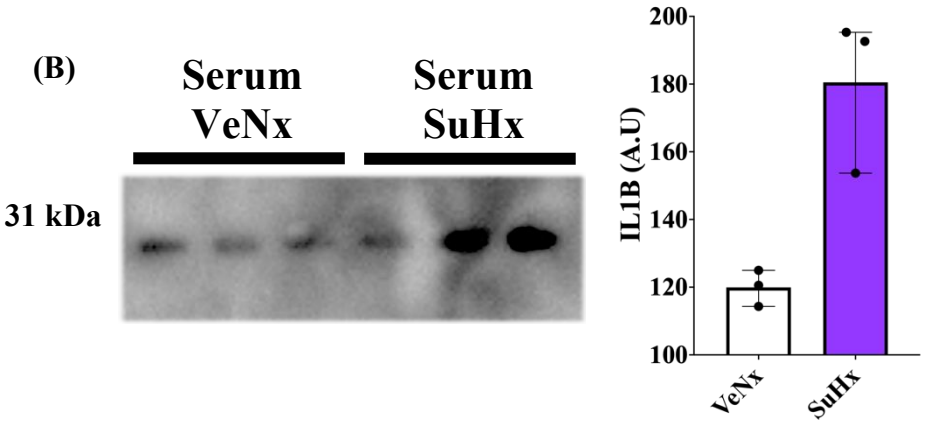

Figure 7B: Western blot analysis of serum IL1β in SuHx model and its control, showing a non-significant increase in IL1β in the serum of SuHx rats rather than VeNx (n=3rats /group; *p=0.1).*

AJRCCM Articles in Press. Published June 14, 2022 as 10.1164/rccm.202110-2274OC

Figure 8

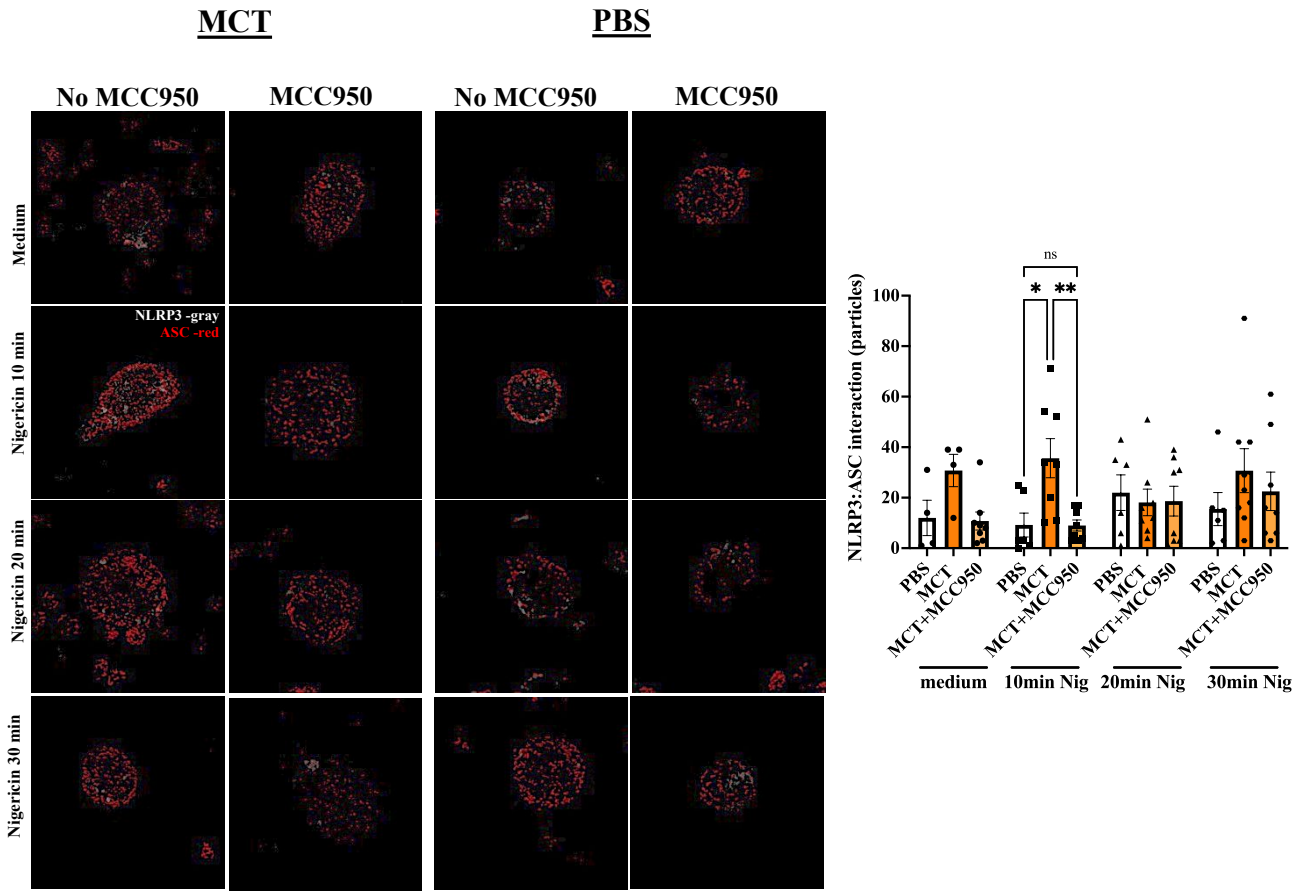

Figure 8: *In vitro* culture of blood monocytes shows components of the NLRP3 inflammasome pathway and illustrates that MCC950 reduces the NLRP3:ASC interaction (NLRP3 (gray) and ASC (red)). Representative images of monocytes enriched from MCT and PBS rats stimulated or not with Nigericin in the presence or absence of MCC950 (n=3 rats/group). Quantification shows that MCT monocytes presented high NLRP3:ASC interaction with Nigericin for 10 minutes (*p= 0.0471*), while the pre-treatment with MCC950 significantly reduced this interaction in 10 minutes (*p= 0.0179*).

AJRCCM Articles in Press. Published June 14, 2022 as 10.1164/rccm.202110-2274OC

Figure 9

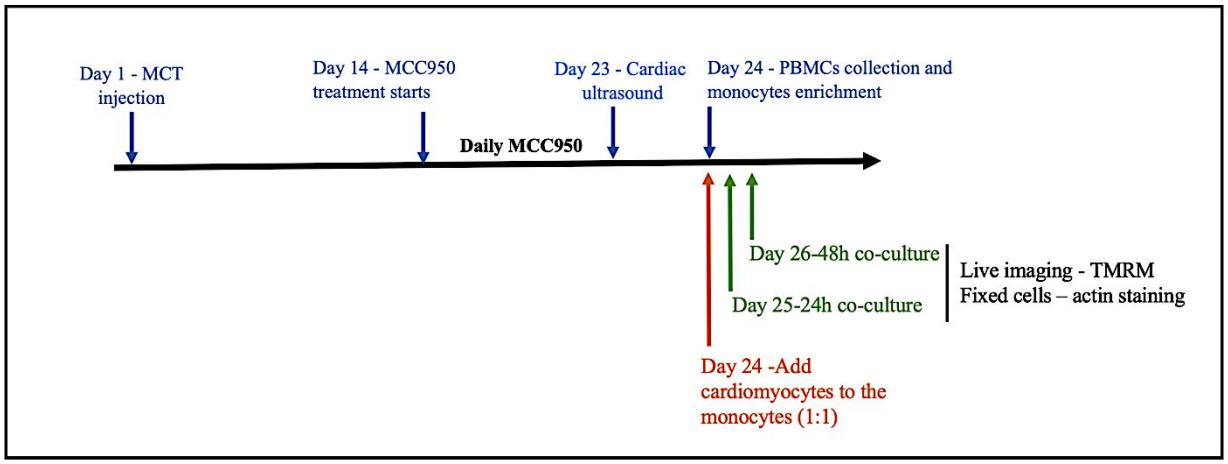

Figure 9: Experimental design of the *in vivo* treatment of MCT and MCC950 followed by enrichment of blood monocytes and co-culture with healthy cardiomyocytes (rat neonatal cardiomyocytes). MCC950 treatment initiated on day 14 after MCT injection, and was administrated daily intravenously (via jugulat catheters). RV function was assessed using ultrasound on the day before the *in vivo* experiment termination. On day 24, 6 ml blood was collected and PBMCs were obtained using Histopaque-1077 followed by enrichment of monocytes. Monocytes were stimulated or not with Nigericin for 10 minutes, washed and cardiomycytes were added to the culture in a proportion of 1:1 (macrophage:cardiomyocyte). After 24 and 48 hours post co-culture, cardiomyocytes were stained with TMRM and live imaging was performed to measure membrane potential. Cells were fixed and stained with phalloidin and DAPI to assess hypertrophy and cell number.

AJRCCM Articles in Press. Published June 14, 2022 as 10.1164/rccm.202110-2274OC

Figure 10

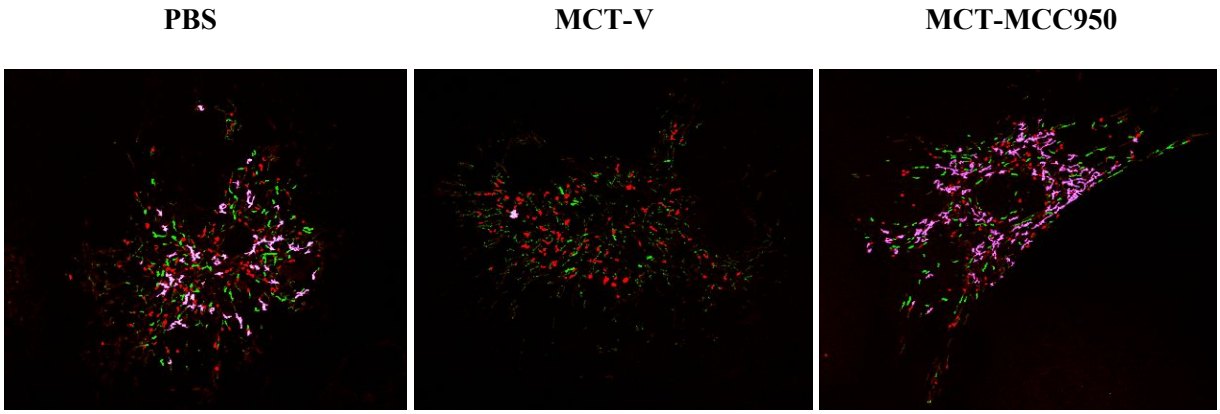

Figure 10: Mitochondrial morphology assessed in nenotal cardiomyocytes that were co-cultured with monocytes (PBS, MCT- and MCC950) and stained with TMRM. Qunatification was conducted using machine learning, an unbiased counting algorithm that trains the computer to classify mitochondria as punctate, intermediate or filamentous. Color code: Green filamentous mitochondria, purple (normal mitochondria) and red (fragmented mitochondria).

AJRCCM Articles in Press. Published June 14, 2022 as 10.1164/rccm.202110-2274OC